




# Measuring the ringdown scalar polarization of gravitational waves in Einstein-scalar-Gauss-Bonnet gravity

Tamara Evstafyeva <sup>1,\*</sup> Michalis Agathos <sup>2,1,†</sup> and Justin L. Ripley <sup>3,1,‡</sup>

<sup>1</sup>*Department of Applied Mathematics and Theoretical Physics, Centre for Mathematical Sciences, University of Cambridge, Wilberforce Road, Cambridge CB3 0WA, United Kingdom*

<sup>2</sup>*Kavli Institute for Cosmology Cambridge, Madingley Road CB3 0HA, Cambridge, UK*

<sup>3</sup>*Illinois Center for Advanced Studies of the Universe & Department of Physics, University of Illinois at Urbana-Champaign, Urbana, Illinois 61801, USA*

(Dated: June 14, 2023)

We model the scalar waves produced during the ringdown stage of binary black hole coalescence in Einstein-scalar-Gauss-Bonnet (EsGB) gravity, using numerical relativity simulations of the theory in the decoupling limit. Through a conformal coupling of the scalar field to the metric in the matter-field action, we show that the gravitational waves in this theory can have a scalar polarization. We model the scalar quasinormal modes of the ringdown signal in EsGB gravity, and quantify the extent to which current and future gravitational wave detectors could observe the spectrum of scalar radiation emitted during the ringdown phase of binary black hole coalescence. We find that within the limits of the theory’s coupling parameters set by current theoretical and observational constraints, the scalar ringdown signal from black hole remnants in the  $10^1 - 10^3 M_\odot$  mass range is expected to be well below the detectability threshold with the current network of gravitational-wave detectors (LIGO-Virgo-KAGRA), but is potentially measurable with next-generation detectors such as the Einstein Telescope.

## I. INTRODUCTION

General relativity (GR) has passed all observational tests to date [1, 2] and, as of 2015, observations of gravitational wave signals in LIGO [3] and Virgo [4] data have been consistent with its predictions [5–10]. Nevertheless, there has been an increasing amount of work that tests the predictions of non-GR theories of gravity (*modified theories of gravity*) with gravitational wave measurements of binary black hole (BH) and neutron star (NS) mergers [11–15]. These *model-dependent* tests of GR have allowed for remarkably strong constraints to be placed on a wide array of modified gravity theories.

Here we focus on the gravitational wave implications for black hole binaries in Einstein-scalar-Gauss-Bonnet (EsGB) gravity. EsGB gravity can be motivated from effective-field-theory-styled arguments [16, 17], and has been shown to appear in the low-energy limits of heterotic string theories [18–20]. What makes EsGB interesting from a phenomenological point of view is that black holes in the theory can have scalar hair [21, 22] (for a review, see [23]). Because of this, binary black hole (BBH) systems can emit scalar radiation [24]. From a theoretical point of view, EsGB gravity is a Horndeski theory [25] and, as such, has second order equations of motion, circumventing the Ostrogradsky instability. In addition, the theory has been shown to have a well-posed initial value problem in the weak coupling limit [17] which allows for numerical relativity simulations of the full theory [26–

29].<sup>1</sup>

In this paper, we focus on the leading order effects of EsGB on the gravitational waveform emitted during the ringdown stage of BBH mergers. It is expected that the strongest constraints on most modified theories of gravity will come from the inspiral, due to the cumulative dephasing of the signal from the GR predicted waveform, over a large number of observed cycles [33, 34]. Nevertheless, correctly modeling the ringdown is crucial to understanding the properties of the remnant black hole formed from binary coalescence, and to performing consistency tests with theory-specific estimates of the final black hole properties inferred from the inspiral and merger [35]. While the dephasing of the inspiral can be a common feature of many different theories of modified gravity and the theory-specific details can be difficult to model at high accuracy (see [13, 36] for perturbative approaches in EsGB), a spectroscopic analysis of the ringdown signal may reveal characteristic features that will help narrow down the origin of an observed deviation from GR.

Working in the decoupling limit of EsGB gravity, we extract first-order tensorial and scalar waveforms and focus on the ringdown portion of the signal. We study the quasinormal mode (QNM) spectrum of the resulting scalar and tensor waveforms and numerically compute the amplitudes of the excited modes. Unlike most previous studies on EsGB gravity, we study the impact of the radiated scalar field on the *scalar polarization* measured

\* te307@cam.ac.uk

† magathos@damtp.cam.ac.uk

‡ ripley@illinois.edu

<sup>1</sup>It is, however, not guaranteed that dynamical spacetimes will preserve the weak coupling of their initial data during their evolution, and local pathologies may form [30–32].

by the gravitational wave detectors, through the presence of a nonminimal scalar field coupling to the metric tensor in the matter field action (without such a coupling, gravitational waves would not have a scalar polarization component in EsGB gravity [37]). While there has been work on model-independent tests of the polarization of gravitational waveforms [38–41], we present the first model-dependent analysis of the feasibility of measuring a nontensor polarization from black hole binaries with current and future gravitational wave detectors (we note though that Ref. [42] considers model-dependent tests with stochastic gravitational wave backgrounds). Ultimately, we find the scalar polarization—given current constraints on the EsGB gravity and weak-field tests of general relativity—is unobservable with current gravitational wave detectors, although there is a higher chance that it could be measured with next-generation detectors.

The paper is organized as follows. In Sec. II A we present the theoretical framework of EsGB gravity in the Einstein frame. In Sec. II B, we review how to extract the polarization content of gravitational waves (GWs), and show how the conformal scalar field coupling can give rise to a scalar polarization in gravitational waves. Next, we review and justify the application of the decoupling limit for solving the equations of motion of EsGB gravity in Sec. II C. For reference, we present a summary of current observational and theoretical constraints on the couplings of the theory we consider in Sec. II D. In Secs. III A–III C we overview our numerical set-up and the diagnostics we used to extract physical quantities from our simulations. In Sec. III D, we present the scalar waveforms measured from our numerical relativity (NR) simulations. We analyse the QNM spectrum of our resulting scalar waveforms in Sec. IV and compute their signal-to-noise ratio (SNR) in Sec. V A to assess the measurability of the scalar signal. We then move on to a full Bayesian data analysis of our simulated signals by performing NR injections of the scalar waveform into simulated current and future-generation detector noise using a tailored ringdown pipeline in Sec. VI. We finish with concluding remarks in Sec. VII.

Our notation and conventions are as follows. The metric signature is  $(-+++)$  and we use  $M$  to denote the Arnowitt-Deser-Misner (ADM) mass. We use lower case Greek indices to index spacetime components (indexed 0, 1, 2, 3, with 0 being the timelike index) and lower case Latin indices to index spatial components. The Riemann tensor is  $R^\alpha{}_{\mu\beta\nu} = \partial_\beta \Gamma^\alpha_{\mu\nu} - \dots$ .

## II. THEORETICAL BACKGROUND

### A. Formulation of four-derivative scalar-tensor ( $4\partial$ ST) gravity

The general action for Einstein-scalar-Gauss-Bonnet gravity is

$$S = \frac{c^4}{16\pi G} \int d^4x \sqrt{-g} [R + X - V(\varphi) + \bar{\alpha}(\varphi) X^2 + \alpha_{\text{GB}} \beta(\varphi) \mathcal{R}_{\text{GB}}] + S_M[\Psi, A^2(\varphi) g_{\mu\nu}], \quad (1)$$

where  $V(\varphi)$  is the scalar field potential,  $\bar{\alpha}(\varphi)$ ,  $\beta(\varphi)$  are arbitrary coupling functions of the scalar field,  $X \equiv -\frac{1}{2}(\nabla\varphi)^2$ ,  $S_M$  is the action functional for the matter fields (which we denote schematically with  $\Psi$ ),  $A^2(\varphi)$  is the conformal coupling of matter to the metric, and  $\mathcal{R}_{\text{GB}}$  is the Gauss-Bonnet scalar

$$\mathcal{R}_{\text{GB}} \equiv \frac{1}{4} \epsilon^{\mu\nu\alpha\beta} \epsilon^{\rho\sigma\gamma\delta} R_{\mu\nu\rho\sigma} R_{\alpha\beta\gamma\delta}. \quad (2)$$

If  $A \neq 0$ , the scalar field couples directly to matter. This coupling generally leads to violations of the weak-equivalence principle (barring the presence of *screening* mechanisms [43]), as the effective gravitational field felt by matter fields will depend on the value of the scalar field  $\varphi$ . Weak field tests of gravity have strongly constrained violations of the weak-equivalence principle, which can be translated to constraints on the strength of the coupling  $A$  [1]. In geometric units, the coupling parameter  $\alpha_{\text{GB}}$  has dimensions length squared,  $L^2$ . It is then natural to expect strong constraints on the scalar Gauss-Bonnet coupling will come from regions of high spacetime curvature [33, 34, 44].

In this work we examine a subset of theories for which  $V = \bar{\alpha} = 0$ . We assume the beyond-GR corrections give only relatively small deviations to the background GR solution. Therefore, we impose that  $|\varphi|, |\alpha_{\text{GB}}|, |\beta| \ll 1$  and to leading order we have

$$S = \frac{c^4}{16\pi G} \int d^4x \sqrt{-g} [R - \frac{1}{2}(\nabla\varphi)^2 + \beta_0 \varphi \mathcal{R}_{\text{GB}}] + S_M[\Psi, (1 + a_0\varphi) g_{\mu\nu}], \quad (3)$$

where we have Taylor expanded  $\beta$  and  $A$  in  $\varphi$ , set  $A(0) = 1$ ,  $A'(0) \equiv a_0/2$ , and  $\beta_0 \equiv \alpha_{\text{GB}}\beta'(0)$ . We have discarded the term  $\beta(0)$  as the Gauss-Bonnet scalar is a total derivative in four spacetime dimensions, so it does not contribute to the equations of motion.

### B. Polarization content

In alternative metric theories of gravity, there may exist up to six polarizations associated with additional degrees of freedom: tensorial (plus and cross), vector ( $x$  and  $y$ ) and scalar (breathing and longitudinal) [45]. Because of their symmetries, the breathing and longitudinal

modes are fully degenerate to networks of quadrupolar antennas [46], so we will refer to them jointly as the scalar polarization. The scalar polarization state is generally a mixture of the transverse breathing and longitudinal polarizations and is excited by a massive scalar field. In the massless limit, the longitudinal polarization disappears, while the breathing one persists [47]. Since the scalar field we consider is massless, we only study the breathing polarization in this work.

The six polarization states are encoded in six ‘‘electric’’ components of the Riemann tensor,  $R_{i0j0}$  ( $i, j$  spatial), which can be written in terms of the following Newman-Penrose scalars [45]

$$\Psi_2 = \frac{1}{6}R_{z0z0}, \quad (4)$$

$$\Psi_3 = \frac{1}{2}(-R_{x0z0} + iR_{y0z0}), \quad (5)$$

$$\Psi_4 = R_{y0y0} - R_{x0x0} + 2iR_{x0y0}, \quad (6)$$

$$\Phi_{22} = -(R_{x0x0} + R_{y0y0}). \quad (7)$$

In Fig. 1 we illustrate the form of the different polarization states. Perturbing the metric and scalar field, the metric  $\hat{g}_{\mu\nu} = (1 + a_0\varphi)g_{\mu\nu}$  that couples to the matter fields (such as a gravitational wave detector) in the wave zone is

$$\hat{g}_{\mu\nu} = \eta_{\mu\nu} + h_{\mu\nu} + a_0\eta_{\mu\nu}\varphi + \dots, \quad (8)$$

where  $\eta_{\mu\nu}$  is the Minkowski metric. The tensorial perturbation  $h_{\mu\nu}$  gives the plus and cross polarizations, while the coupling constant  $a_0$ , along with a nonzero value of  $\varphi$ , gives a new scalar breathing-mode polarization to gravitational waves<sup>2</sup> [42, 48].

### C. Perturbative equations of motion

Unless otherwise stated, in this section we work in geometric units  $G = c = 1$ . Our discussion roughly follows that of [49, 50]. We start with the full equations of motion derived from action (3)

$$G_{\mu\nu} = \frac{1}{2}T_{\mu\nu} - \beta_0 C_{\mu\nu}^{\text{GB}}, \quad (9)$$

$$\square\varphi = -\beta_0\mathcal{R}_{\text{GB}}, \quad (10)$$

where

$$T_{\mu\nu} = \nabla_\mu\varphi\nabla_\nu\varphi - \frac{1}{2}g_{\mu\nu}\nabla_\rho\nabla^\rho\varphi, \quad (11)$$

$$C_{\mu\nu}^{\text{GB}} = 2g_{\rho(\mu}g_{\nu)\alpha}\epsilon^{\kappa\alpha\tau\eta}\nabla_\lambda(*R^{\rho\lambda}{}_{\tau\eta}\nabla^\kappa\varphi). \quad (12)$$

<sup>2</sup>We note that if  $a_0 = 0$ , then gravitational waves have no scalar polarization in EsGB gravity [37].

We expand the metric and the scalar field as

$$\varphi = \sum_{k=0}^{\infty} \frac{1}{k!} \epsilon^k \varphi^{(k)}, \quad (13)$$

$$g_{\mu\nu} = g_{\mu\nu}^{(0)} + \sum_{k=1}^{\infty} \frac{1}{k!} \epsilon^k h_{\mu\nu}^{(k)}. \quad (14)$$

where  $\epsilon$  is a book-keeping parameter for our perturbative expansion. By considering the equations of motion order by order in  $\epsilon$ , one finds that up to  $\mathcal{O}(\epsilon)$  [50]

$$\varphi^{(0)} = 0, \quad g_{\mu\nu}^{(0)} = g_{\mu\nu}^{\text{GR}}, \quad (15)$$

$$\varphi^{(1)} = \varphi^{(1)}, \quad h_{\mu\nu}^{(1)} = 0. \quad (16)$$

We note that the zeroth order equations of motion are the Einstein field equations minimally coupled to a massless scalar field. The choice of  $\varphi^{(0)} = 0$  in the zeroth order solution (15) is motivated by the fact that asymptotically flat black holes cannot carry scalar hair [51], which if initially present would be radiated away at late times, and that a cosmological value of  $\phi$  for EsGB gravity has been constrained by measurements of the speed of gravitational waves [12, 52]. Using Eqs. (15) and (16), the equations of motion to  $\mathcal{O}(\epsilon)$  reduce to

$$G_{\mu\nu}^{(0)} = 0, \quad (17)$$

$$\square^{(0)}\varphi^{(1)} = -\mathcal{R}_{\text{GB}}^{(0)}\beta_0. \quad (18)$$

We note that there is no backreaction of the scalar field on the background geometry, however at  $\mathcal{O}(\epsilon^2)$  the metric will be corrected by the backreaction of the scalar field  $\varphi^{(0)}$  on the spacetime [50, 53, 54].

We reintroduce dimensions by choosing the characteristic length scale of the system to be  $L$ , and introduce a dimensionless coordinate  $\hat{x} = Lx$ . By redefining  $x \rightarrow \hat{x}$ , we acquire a factor of  $L^{-2}$  in front of the wave operator and a factor of  $L^{-4}$  in front of the Gauss-Bonnet scalar, leading to

$$\hat{\square}^{(0)}\varphi^{(1)} = -\beta_0 L^{-2} \hat{\mathcal{R}}_{\text{GB}}^{(0)}. \quad (19)$$

We then may rescale the scalar field

$$\varphi^{(1)} = \left(\frac{\beta_0}{L^2}\right) \hat{\varphi}, \quad (20)$$

so that

$$\hat{\square}^{(0)}\hat{\varphi} = -\hat{\mathcal{R}}_{\text{GB}}^{(0)}. \quad (21)$$

This implies that a solution with a given  $\beta_0/L^2$  parametrizes a family of solutions with different  $L$  and  $\beta_0$ . Further, Eq. (20) naturally introduces the choice for the dimensionless parameter  $\epsilon$ , which we use to parametrize the weak coupling of our solutions. Since we are interested in binary black hole systems and the corrections become larger for smaller masses, we choose  $L = m_1$ ,

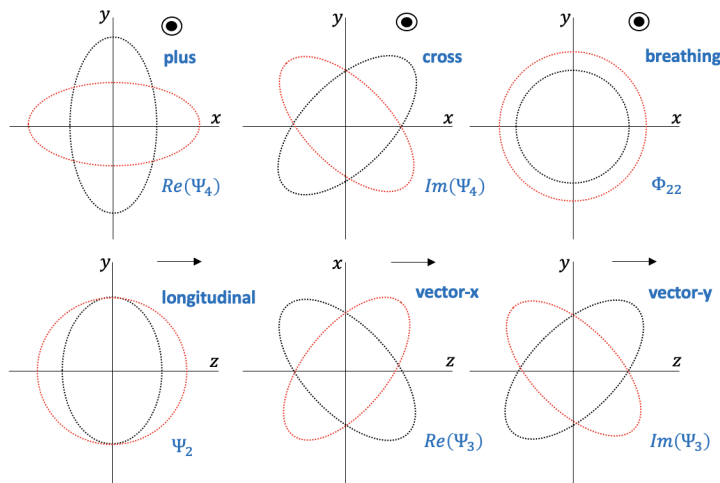


FIG. 1: The classification of the six polarizations encoded in the four Newman-Penrose scalars. The shapes represent displacement that each mode induces on a sphere of test particles. The wave is assumed to propagate in the  $z$ -direction indicated by the icons/arrows in the right corners.

which is the mass of the smaller black hole in our binary black hole configuration. We then define

$$\epsilon \equiv \frac{\beta_0}{m_1^2} \ll 1. \quad (22)$$

By combining Eqs. (20) and (8), we note that the scalar GW amplitude is then controlled by the couplings of our theory via  $a_0\beta_0/m_1^2$ . The dimensionless EsGB parameter  $\epsilon$  plays an important role in EsGB gravity. Depending on the coupling  $\beta_0$  chosen in the theory, a stationary BH solution of mass  $m_1$  cannot exist above a certain threshold  $\max(\beta_0/m_1^2) = \epsilon_{\text{thr}} > \epsilon$ . Such threshold is controlled by the regularity of the scalar field on the horizon and the finite radius singularity being hidden behind it for sufficiently small  $\beta_0$ . If the coupling becomes too large, a naked singularity emerges from within the horizon in solutions to the full theory. For instance, in the spherical-symmetric case of shift-symmetric EsGB,  $\epsilon_{\text{thr}} \sim 0.3$  [22]. Hyperbolicity constraints on the theory suggest a somewhat more stringent bound of  $\epsilon_{\text{thr}} \sim 0.2$  [55]. In Fig. 2, we outline schematically the range of validity of our EsGB theory in the parameter space of  $a_0 \times \beta_0/m_1^2$ , taking into consideration the observational constraints on  $a_0$  from Table I and theoretical constraints on  $\beta_0/m_1^2$ . The contour lines therefore represent possible scalar GW amplitude values.

#### D. Current observational constraints

Here we discuss current experimental tests and observational bounds on the parameters  $a_0$  and  $\beta_0$ . The EsGB coupling  $\beta_0$  has been most strongly constrained through the analysis of inspiral and merger of binary systems of compact objects using GW data released by the

LIGO-Virgo-KAGRA (LVK) collaboration [56]. Weak-field tests of GR also place a constraint on the coupling, but do not constrain it as significantly [57], as the Gauss-Bonnet coupling does not lead to much scalarization of stellar solutions [24]. This being said, as we are considering  $a_0 \neq 0$ , stars can scalarize in the theory we consider. In this work, we use the first constraint on  $a_0$ , obtained from the Viking relativity experiment on verification of signal retardation by solar gravity [58]<sup>3</sup>,  $a_0^2 \lesssim 10^{-3}$ . Table I references the studies constraining the EsGB coupling<sup>4</sup>  $\beta_0$  and the conformal coupling  $a_0$ . We additionally summarize theoretical constraints on the dimensionless coupling  $\beta_0/m_1^2$  as discussed in Sec. II C.

### III. NUMERICAL SETUP

#### A. Numerical relativity code and evolution equations

Here we describe our numerical set-up to solve Eqs. (17) and (18). For our simulations, we use a modified version of **GRChombo** [70–72], which is a publicly available finite difference numerical relativity code built on the **Chombo** [73] adaptive mesh refinement libraries. The

<sup>3</sup>We note however that the most stringent constraint of  $a_0^2 \lesssim 10^{-5}$  is known to be from the Cassini measurements of the Shapiro time delay [1, 59]. Here we use a weaker constraint from the Viking experiment to see how well in principle the scalar polarization could be measured by present GW detectors.

<sup>4</sup>If one assumes that both objects in GW190814 are BHs, then an even more stringent constraint on the EsGB coupling can be found [60]. However, in this work we take a conservative approach, by quoting the constraints from GW190814 that assume the secondary object is a neutron star.

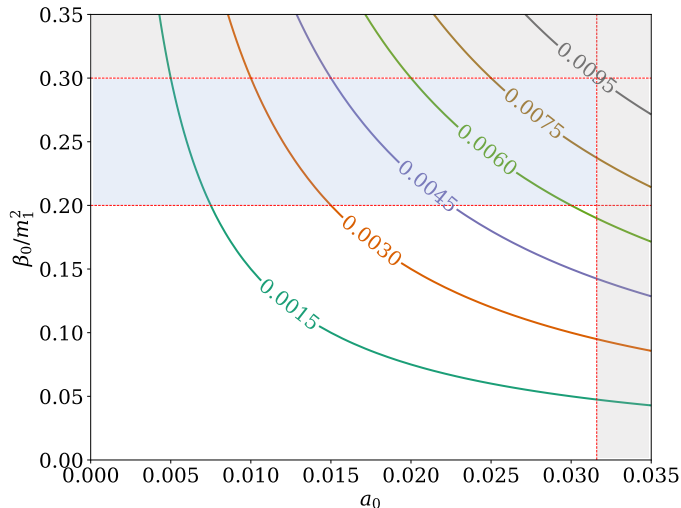


FIG. 2: Range of validity of our EsGB theory, taking into account theoretical constraints on the dimensionless coupling  $\beta_0/m_1^2$  and experimental constraint on the conformal factor  $a_0$ . The vertical dashed line separates the maximally allowed value of  $a_0$  (to the left) from the observationally ruled out values (shaded gray region to the right). The two horizontal lines indicate the two theoretical constraints on the value of  $\beta_0/m_1^2$ . The upper line at  $\beta_0/m_1^2 = 0.3$  represents the maximum coupling allowed before naked singularities appear in static solutions to the theory, while the line at  $\beta_0/m_1^2 = 0.2$  represents the upper bound before the theory suffers a breakdown in hyperbolicity. See Secs. IIC and IID for more discussion.

Coupling $\sqrt{\beta_0}$			
Study	References	Constraint	
Solar system constraints	[57]	$\mathcal{O}(10^7)$ km	
GW150914 ppE	[61]	$\lesssim 72.85$ km	
EsGB constraints from LIGO/Virgo events and ParSpec formalism	[62]	$\lesssim 35$ km	
EsGB constraints from EOB waveform model and ParSpec formalism	[63]	$\lesssim 35$ km	
X-ray binary orbital decay	[64]	$\lesssim 14.1$ km	
LIGO SNR 30 detections (projection)	[65]	$\mathcal{O}(1 - 10)$ km	
Second order EdGB simulations for GW150914	[53]	$\lesssim 15.6$ km	
Compact star stability	[66]	$\lesssim 7.6$ km	
First order EdGB scalar simulations for GW151226	[67]	$\lesssim 3.8$ km	
EsGB constraints from BHBH GW events	[14]	$\lesssim 1.7$ km	
EsGB constraints from BHNS GW events (GW200105, GW200115 and GW190814)	[56]	$\lesssim 1.18$ km	
Coupling $a_0$			
Viking relativity experiment on signal retardation	[58, 68]	$\sqrt{10^{-3}}$	
VBLI measurement of solar gravitational deflection	[69]	$\sqrt{10^{-4}}$	
Cassini Shapiro time delay	[1, 59]	$\sqrt{10^{-5}}$	
Theoretical constraints on $\beta_0/m_1^2$			
Shift-symmetric EsGB in spherical symmetry	[22]	$\lesssim 0.3$	
Scalarized black holes in the full dynamical EdGB gravity	[55]	$\lesssim 0.2$	

TABLE I: Summary of current constraints on the EsGB coupling parameter  $\beta_0$ , the dimensionless parameter  $\beta_0/m_1^2$  and the conformal coupling  $a_0$  (c.f. [53]). Our conventions for  $\beta_0$  and  $a_0$  are given in Eq. (3).

metric and the scalar field are evolved with the method of lines using fourth order finite difference stencils and Runge Kutta time integration. We use the covariant and conformal Z4 (CCZ4) formulation [74] with the moving puncture gauge [75, 76] for evolving the Einstein equations (17). The evolution equations for the Einstein field equations in the CCZ4 formulation can be found in Sec. III F of [77], where we replace  $\kappa_1 \rightarrow \kappa_1/\alpha$ , in

order to stably evolve BHs, and choose the constraint damping parameters to be  $\kappa_1 = 0.1$ ,  $\kappa_2 = 0$  and  $\kappa_3 = 1$ .

The evolution equations for the scalar field (18) read

$$\begin{aligned}\partial_t \varphi &= \alpha \Pi + \beta^i \partial_i \varphi, \\ \partial_t \Pi &= \alpha K \Pi + \beta^i \partial_i \Pi \\ &\quad + \tilde{\gamma}^{km} \left( \chi \alpha \partial_k \partial_m \varphi + \chi \partial_m \alpha \partial_k \varphi - \frac{1}{2} \alpha \partial_m \chi \partial_k \varphi \right) \\ &\quad - \chi \alpha \tilde{\gamma}^{ij} \tilde{\Gamma}_{ij}^k \partial_k \varphi + \alpha (\beta_0 \mathcal{R}_{\text{GB}}),\end{aligned}\quad (23)$$

where  $\Pi \equiv -1/\alpha(\partial_t \varphi - \beta^m \partial_m \varphi)$ ,  $\alpha$  is the lapse function,  $\beta^i$  is the shift vector,  $\tilde{\gamma}_{ij} \equiv \chi \gamma_{ij}$  is the conformally rescaled metric constituent of the conformal factor  $\chi = \det(\gamma_{ij})^{-1/3}$  and physical spatial metric  $\gamma_{ij}$ . We rewrite the Gauss-Bonnet scalar in the gravito-electric,  $E_{ij}$ , and gravito-magnetic,  $B_{ij}$ , counterparts [50]

$$\mathcal{R}^{\text{GB}} = 8(E^{kl} E_{kl} - B_{kl} B^{kl}), \quad (25)$$

where in CCZ4 variables they take the form of [72]

$$\begin{aligned}E_{ij} &= [\mathcal{R}_{ij} - K^s{}_i K_{js} + K_{ij}(K - \Theta) + D_{(i} \Theta_{j)}]^{TF}, \\ B_{kl} &= \epsilon_{ks(i} D^s K_{j)}{}^k.\end{aligned}\quad (26)$$

Here  $\mathcal{R}_{ij}$  is the 3D Ricci tensor,  $K_{ij}$  is the extrinsic curvature,  $\Theta = -n_\mu Z^\mu$  is the projection of the CCZ4 vector  $Z^\mu$  onto the timelike unit normal  $n^\mu$ ,  $[\dots]^{TF}$  denotes the tracefree part and  $D_i$  is the covariant derivative compatible with the physical metric  $\gamma_{ij}$ . In the case of  $\Theta = 0$ , we recover the Baumgarte-Shapiro-Shibata-Nakamura-Oohara-Kojima formulation [78–80].

## B. Grid setup and initial data

For the results presented in this paper we set up a computational domain of size  $1024M$ . We use a grid spacing of  $\Delta x = 2M$  in the outermost refinement level with eight additional refinement levels and a Courant factor of 1/4. In this setup we roughly have 64 points covering the smallest BH in the most asymmetric run (mass ratio 1:2). For boundary conditions, we use Sommerfeld boundary conditions and take advantage of the bitant symmetry to evolve only half of the grid. To validate our results, we estimated the discretization error for the amplitudes of  $\Psi_4$  and  $\varphi$  to be  $\lesssim 2\%$  and for phase of  $\Psi_4$  to be  $\lesssim 0.15$  radians. We further estimate the finite radius extraction error to be  $\lesssim 2\%$  and thus a total error budget of  $\lesssim 4\%$ . See Figs. 14–16 of Appendix A 1 for a quantitative illustration of the convergence of the code.

For our initial data, we consider two nonspinning black holes with initial masses  $m_1$  and  $m_2$  (we assume  $m_2 > m_1$ ), initial linear momenta  $\mathbf{P}_1$  and  $\mathbf{P}_2$  and initial separation  $D$ . We prescribe quasicircular initial data for a black hole binary by using puncture initial data [81] of Bowen-York [82] type provided by the spectral initial data solver `TwoPunctures` [83, 84].

We have investigated the effects of different initial separations on the eccentricity and found that  $D = 8M$

(resulting in four orbits) gave us an eccentricity estimator of no more than 0.012 for all of the configurations considered here (we used Eq. (20) of [85] to calculate the eccentricity).

The initial data for the scalar field is chosen to be  $\varphi = 0$  and  $\partial_t \varphi = 0$ . The authors in [50] found that using an initially vanishing scalar or superposing two hairy solutions gave identical results after sufficiently long evolution (see Fig.4 of [50]). Moreover, this choice of initial data solves the exact constraint equations of EsGB gravity [26, 29]. We therefore do not investigate any other forms of initial data for the scalar field. We further pick three configurations for black holes of different mass ratios  $q = m_1/m_2$ , ( $q \leq 1$ ) summarized in Table II.

## C. Extraction of physical quantities

To order  $\mathcal{O}(\epsilon)$ , the metric sector of our spacetime is determined by the Einstein equations of GR (see Eq. (17)), so that the gravitational waveform will be no different from GR. To calculate gravitational radiation we use the Newman-Penrose formalism [86, 87], and determine the outgoing gravitational radiation by computing complex scalar  $\Psi_4$ . By interpolating the real and imaginary parts of  $\Psi_4$  onto a sphere of fixed radius  $R_{\text{ext}} = 110M$ , we decompose them in terms of spin-weighted spherical harmonics  $Y_{lm}^s$  with  $s = -2$  [88, 89],

$$\Psi_{4,lm}(t, R) = \int_{S^2} \Psi_4(t, R, \theta, \phi) \overline{Y_{lm}^{-2}}(\theta, \phi) d\Omega, \quad (27)$$

where  $d\Omega = \sin \theta d\theta d\phi$ . By similar decomposition into spherical harmonics  $Y_{lm}$  and integrating over the sphere, we construct the scalar waveform

$$\varphi_{lm}(t, R) = \int_{S^2} \varphi(t, R, \theta, \phi) \overline{Y_{lm}}(\theta, \phi) d\Omega. \quad (28)$$

In what follows, we use the subscript “rad” to denote quantities calculated from the start of our simulation, which includes spurious “junk” radiation. Otherwise, we consider quantities from  $t = R_{\text{ext}} + 50M$  onwards. The mass and spin of the final BH are estimated from balance arguments [90]

$$M_{\text{fin}} = M_{\text{ADM}} - E_{\text{rad}}^{\text{GW}}, \quad (29)$$

$$j_{\text{fin}} = \frac{L - J_{\text{rad}}^z}{M_{\text{fin}}^2}, \quad (30)$$

where  $E_{\text{rad}}^{\text{GW}}$  denotes the total radiated energy of GWs,  $J_{\text{rad}}^z$  is the radiated angular momentum in the  $z$  direction (by symmetry) and  $L = P_y D$ . In the above balance arguments the radiated energy and angular momentum

Run	$q$	$m_1$	$m_2$	$\mathbf{P}_1$	$\mathbf{P}_2$	$M_{\text{fin}}$	$j_{\text{fin}}$	$j_{\text{fin}}/M_{\text{fin}}$
BBH-11	1	0.5	0.5	(-0.0013 -0.11 0.0)	(0.0013 0.11 0.0)	0.9511	0.69	0.7255
BBH-23	2/3	0.4	0.6	(-0.0012 -0.108 0.0)	(0.0012 0.108 0.0)	0.9549	0.67	0.7016
BBH-12	1/2	0.33	0.67	(-0.0011 -0.1001 0.0)	(0.0011 0.1001 0.0)	0.9611	0.62	0.6451

TABLE II: Two puncture initial data used for three binary BH configurations considered in this paper.  $M_{\text{fin}}$  and  $j_{\text{fin}}$  denote the final mass and final spin of the remnant BHs respectively, which were calculated from balance arguments given in Eqs. (29) and (30). We estimate 0.01% error in the final mass and 0.05% error in the final spin when compared to their Richardson-extrapolated values. In Appendix A 2 we present convergence plots for the radiated energy and angular momentum.

are determined through [91, 92]

$$E_{\text{rad}}^{\text{GW}}(t) = \lim_{r \rightarrow \infty} \frac{r^2}{16\pi} \int_{t_0}^t dt' \oint_{S^2} d\Omega \mathbf{e}_r \left| \int_{-\infty}^{t'} dt'' \Psi_4 \right|^2, \quad (31)$$

$$\mathbf{J}_{\text{rad}}(t) = - \lim_{r \rightarrow \infty} \frac{r^2}{16\pi} \text{Re} \int_{t_0}^t dt' \left\{ \oint_{S^2} \left( \int_{-\infty}^{t'} dt'' \Psi_4^* \right) \times \mathbf{J} \left( \int_{-\infty}^{t'} dt'' \int_{-\infty}^{t''} dt''' \Psi_4 \right) d\Omega \right\}, \quad (32)$$

where  $\mathbf{e}_r$  is the unit radial vector of a sphere and  $\mathbf{J}$  is the angular momentum operator for spin weight  $s = -2$

$$\mathbf{J} = \left( \text{Re}\mathbf{J}_+, \text{Im}\mathbf{J}_+, \frac{\partial}{\partial\phi} \right), \quad (33)$$

$$\mathbf{J}_+ = e^{i\phi} \left( i \frac{\partial}{\partial\theta} - \cot\theta \frac{\partial}{\partial\phi} + 2i \csc\theta \right). \quad (34)$$

Apart from tensor energy, we expect some of the scalar field energy to be emitted too. Since the scalar field is of order  $\varphi \sim \epsilon$ , the radiated energy must be of order  $E^\varphi \sim \epsilon^2$ . We note that if we were to continue the order reduction scheme for our solution to  $\mathcal{O}(\epsilon^2)$ , there would be an additional radiated tensor energy sourced by  $\mathcal{O}(\epsilon^2)$  corrections. At least in post-Newtonian (PN) theory this term is suppressed compared to the scalar radiation, so we will ignore it as it is done in [49, 50]. The energy flux of the scalar field through a two-sphere of radius  $R$  is given via

$$\frac{dE^\varphi}{dt} = \int_{S_R^2} T_{ab}^{(\varphi)} n^a dS^b, \quad (35)$$

where  $n^a$  is the timelike unit normal and  $T_{ab}^{(\varphi)} = \frac{1}{2}T_{ab} - \beta_0 C_{ab}^{\text{GB}}$  representing the right hand side of the modified Einstein's equations in Eq. (9). Assuming that a spherical surface is located in the radiation zone of an asymptotically flat spacetime and  $\varphi$  behaves as outgoing radiation in the radiation zone, to leading order we find that  $T_{ab}^{(\varphi)} = \frac{1}{2}T_{ab}$ . Then, to leading order Eq. (35) reads

$$\frac{dE_0^\varphi}{dt} = - \int_{S^2} r^2 T_t^r d\Omega = \int_{S^2} [\dot{\varphi}(t-r)]^2 d\Omega, \quad (36)$$

where the dot denotes time differentiation. We therefore integrate Eq. (36) to find the total radiated scalar energy to leading order.

#### D. Numerical results: Scalar waveforms

In this section we present our numerical results. The initial data for the simulations are listed in Table II. We find good agreement with numerical results of [67], which made use of the same decoupling approximation as we do. We show scalar waveforms for  $l \geq 1$  modes in Fig. 3 and for  $l = 0$  mode in Fig. 4, where we align the waveforms so that the amplitude peaks of the scalar field coincide at  $\hat{t} = 0$  and choose  $\beta_0/m_1^2$  for convenience.

For equal-mass binaries we have only even  $l$ -modes present in the waveform, as equal-mass nonspinning binaries are symmetric under parity transformations ( $\vec{r} \rightarrow -\vec{r}$ ). Since  $Y_{l=\text{odd}}^m(\vartheta, \varphi)$  is antisymmetric and the EsGB coupling is invariant under parity, there must be no emission from odd  $l$ -modes for equal-mass binaries. On the other hand, in the unequal-mass case, odd  $l$ -modes are present and the dipole emission dominates all other higher modes of the scalar waveform for EsGB gravity (it enters at  $-1\text{PN}$  order) [24, 36, 93]. In Fig. 4, we see that the  $l = 0$  mode looks unlike the other modes and is roughly constant before merger time (this is consistent with leading order PN theory [24, 67]). After merger it settles to almost the same value for all the mass ratios, since the remnant BHs formed have quite similar final masses and spins, and thus the same amount of remnant scalar hair. Overall, from Figs. 3 and 4, at fixed  $\beta_0/m_1^2$ , the scalar field radiation becomes stronger for more extreme unequal-mass binaries, especially in the inspiral and merger portions of the signal. End state BHs with smaller spin (*i.e.* BHs formed from more extreme mass ratios) have faster damping times than BHs with higher spin. As a result, the scalar waves in the ringdown are more pronounced at late times for black holes produced from more symmetric-mass-ratio ( $q \sim 1$ ) progenitors. To illustrate this point, we align the (22) modes in the amplitude peak of the scalar field for different mass ratios in Fig. 5, and zoom-in on the ringdown, where the amplitude for more symmetric-mass-ratio binaries becomes larger than for more asymmetric systems later in time.

Finally, the scalar energy flux, as computed from

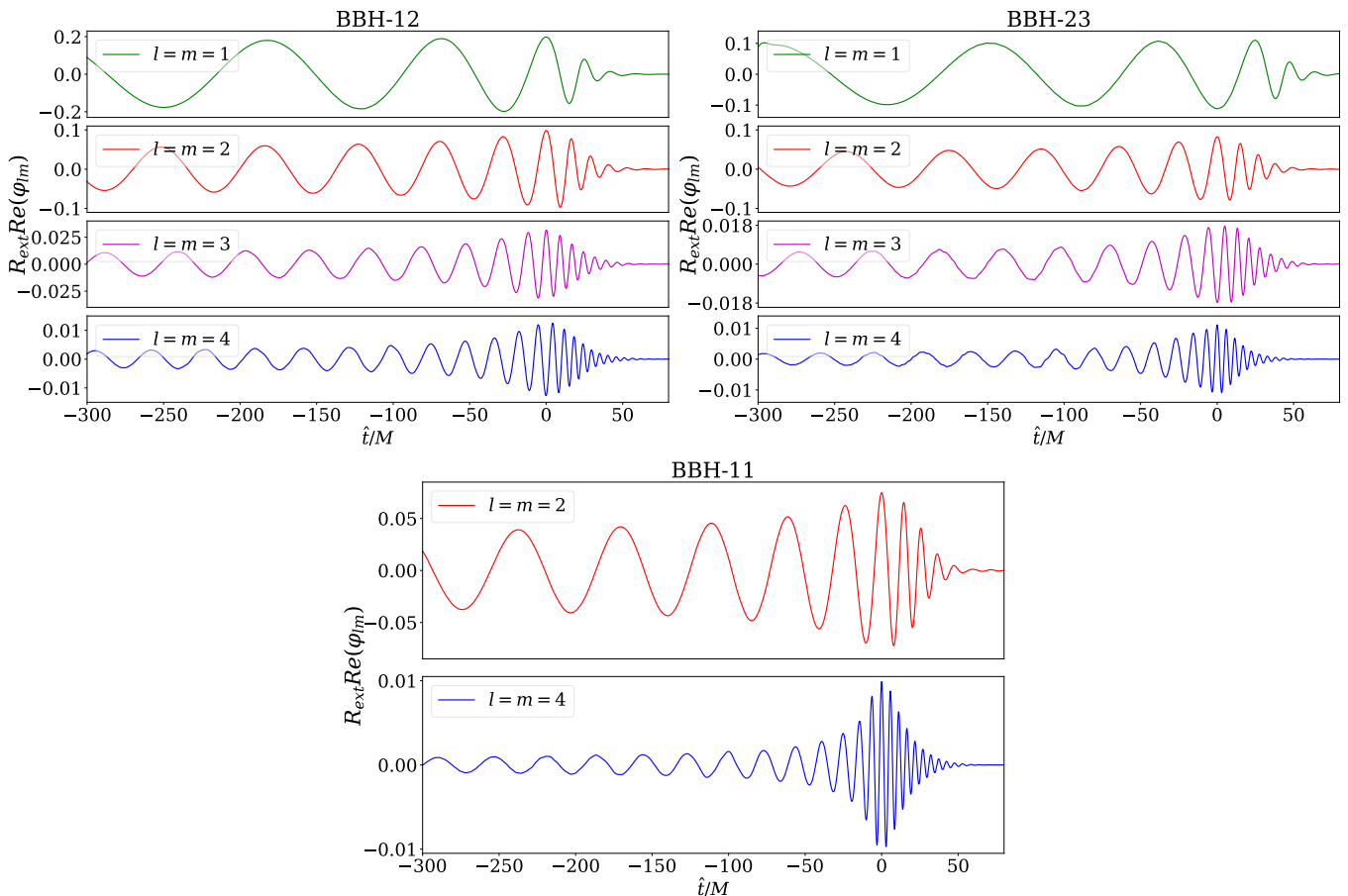


FIG. 3: Scalar waveforms for  $l \geq 1$  for mass ratios of  $q = 1, 2/3, 1/2$  extracted at  $R_{\text{ext}} = 110$ . For unequal mass cases, the scalar field amplitude is more pronounced. The waveforms have been aligned so that the amplitude peaks of the scalar field coincide at  $\hat{t} = 0$ , and we set  $\beta_0/m_1^2 = 1$  for convenience (recall that since we are using an order-reduction scheme, there is no restriction on the value of  $\beta_0/m_1^2$  in our evolution). In our analysis, we choose a physically allowed value of  $\beta_0/m^2$  and rescale the scalar waveforms using Eq. (20).

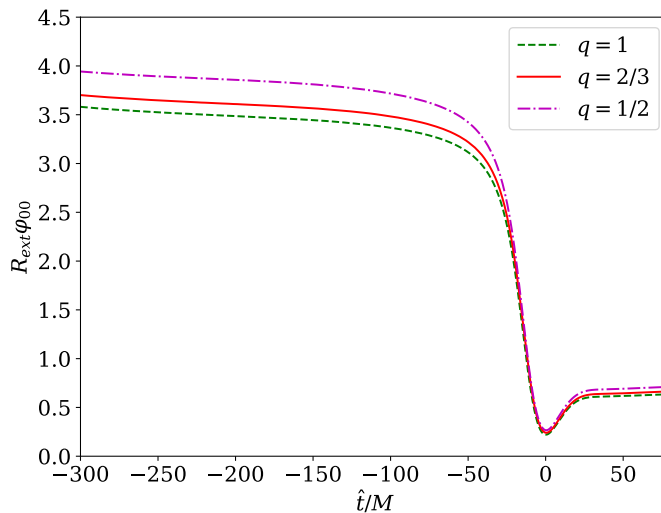


FIG. 4: Scalar  $l = 0$  mode for binary mass ratios of  $q = 1, 2/3, 1/2$ , extracted at  $R_{\text{ext}} = 110$ .

Eq. (36), is shown in Fig. 6. We see that it is dominated by the contribution from  $l = 0$  mode, which is larger



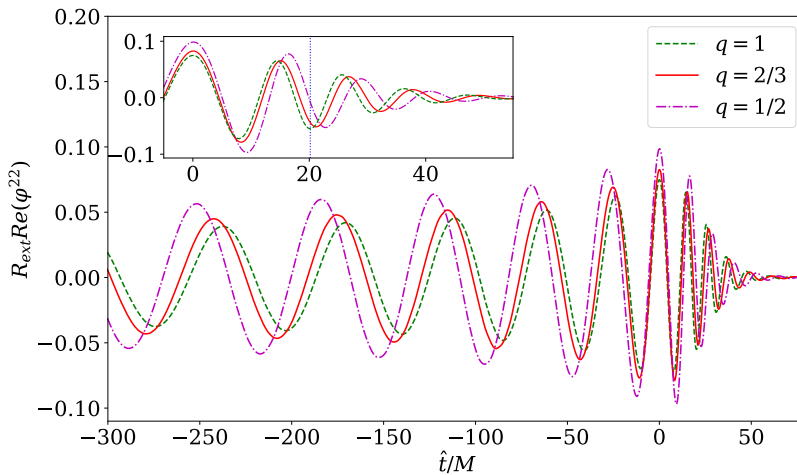


FIG. 5: Scalar  $l = 2, m = 2$  mode for mass ratios of  $q = 1, 2/3, 1/2$ . The inset shows the zoom-in on the ringdown portion of the signal. Within the inset, the blue dotted line indicates the time where the amplitudes of the  $q = 2/3$  and  $q = 1/2$  waveforms become smaller in amplitude than the  $q = 1$  waveform.

for more unequal-mass-ratio binaries, as expected from PN theory [24, 67]. This is unlike the tensorial gravitational energy flux, where the strongest flux comes from the equal-mass binary. This can be explained by the fact that to leading order the total radiated gravitational energy  $E_{\text{rad}}^{\text{GW}} \sim \eta^2$ , where  $\eta = q/(1+q)^2$  is the symmetric mass ratio [94]. We note that the scalar energy flux measured here using Eq. (36) is the second-order effect and so is significantly suppressed—at merger, it accounts for much less than 1% of the gravitational energy flux.

#### IV. MODELING THE SCALAR RINGDOWN WAVEFORM

When exploring the GW phenomenology of astrophysical systems in modified gravity, the ultimate aim is to obtain an accurate waveform model for the signal (here the scalar ringdown) and to be in a position to observe the effects in question and infer information on the underlying theory from the observed GW data. In this section we model the scalar ringdown based on the NR data of Sec. III D. The gravitational waves emitted by the remnant BH formed by a merger, known as the ringdown signal, can be approximated as a superposition of damped sinusoids [95]. In GR, each mode of the tensorial ringdown signals can then be written as

$$h^{lm} = \sum_{J=1}^N H_J e^{-i(\omega_J^{\text{GR}}(t-t_0)+p_J)}, \quad (37)$$

where  $t_0$  is the start time of the ringdown,  $J = (lmn)$  is the mode number,  $H_J$  and  $p_J$  are real amplitude and phase of mode  $J$  at  $t = t_0$ , (which depend on the binary configuration and dynamics near merger), and  $\omega_J$  are the complex frequencies of the  $N$  most dominant QNMs. In a

similar fashion, the scalar ringdown signal can be written as,

$$\varphi_{lm} = \sum_{J=1}^N A_J e^{-i(\omega_J^{\text{GR}}(t-t_0)+p_J)}, \quad (38)$$

where  $A_J$  now denote scalar real amplitudes. For a mode  $J$  corresponding to a given set of QNM indices  $(lmn)$ , we write the real and imaginary parts as

$$\omega_{\text{QNM}} = \omega_{lmn} - \frac{i}{\tau_{lmn}}. \quad (39)$$

The integers  $(lm)$  describe the angular properties of the emission, while  $n$  is the overtone number [96]. Modes with  $n = 0$  are referred to as the *fundamental modes*, while with  $n \geq 1$  as *overtones*, which (at least in GR) have lower frequencies and greater damping times than their corresponding fundamental modes. We have denoted the total number of quasinormal modes with which we model the ringdown signal by  $N$ .

The no-hair theorem of GR states that the damping times,  $\tau^{lmn}$ , and frequencies,  $\omega^{lmn}$ , for gravitational wave perturbations around astrophysical (noncharged) BHs in GR, are uniquely determined by the mass and spin of the final black hole. The excitation coefficients also depend on the initial conditions of the perturbation [96], in our case the progenitor parameters. For modified theories of gravity, the QNM spectrum of BH spacetimes generally depends on the theory in question, and so observations of the ringdown signal can provide a way to discriminate between GR and possible modified theories of gravity. Unlike GR [97], for alternative theories of gravity there is typically no set of separable master equations for linearized perturbations of black holes. Instead, the calculation of QNMs has relied on either the assumption of spherical symmetry [98, 99], the slow spin approxi-

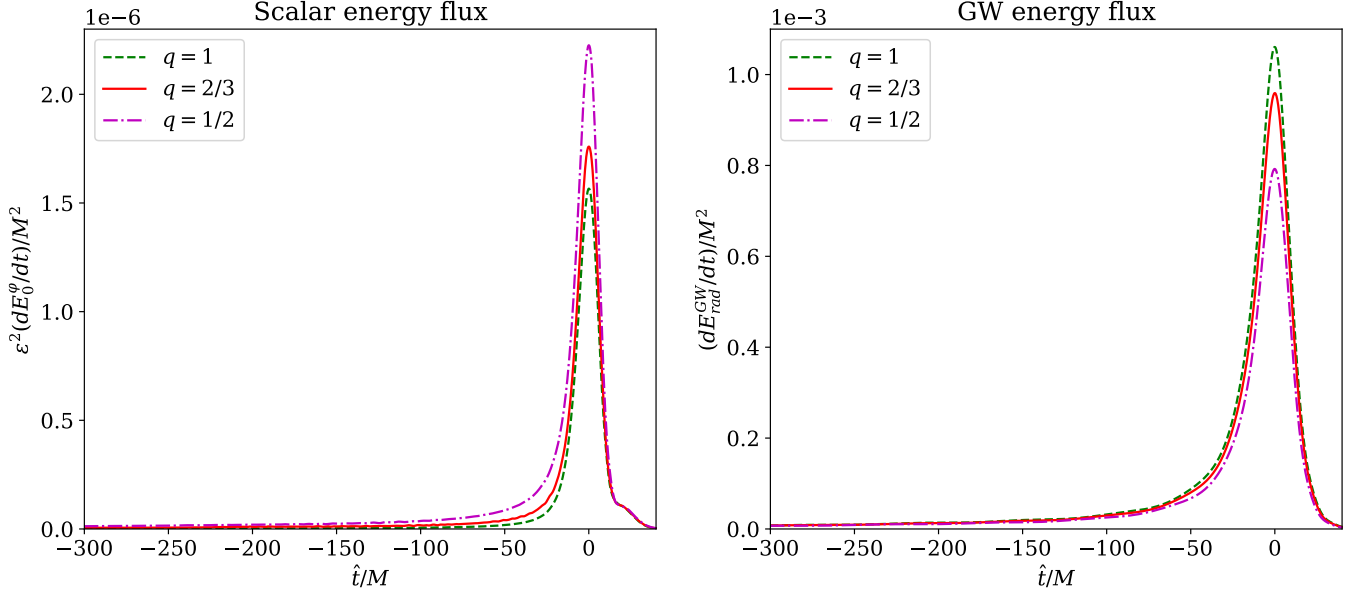


FIG. 6: *Left*: scalar energy flux computed using Eq. (36). As in Fig. 3, we set  $\beta_0/m_1^2 = 1$ . *Right*: gravitational wave energy flux computed using Eq. (31).

mation [100, 101],<sup>5</sup> or on numerical fits of time-domain waveforms computed from NR simulations [50, 103]. In this work we focus on the last method by performing numerical fits to the scalar and tensor waveforms.

In our analysis, we take a similar approach of modeling the scalar ringdown as a superposition of damped sinusoids given by Eq. (38), except our QNM frequencies no longer correspond to just scalar QNMs of GR. We note that the operator acting on  $\varphi$  in its equation of motion consists of the background GR metric in the decoupling approximation we use (see Eq. (18)). Therefore, the homogeneous solution of the beyond-GR scalar perturbation equation around a BH spacetime should contain the same scalar QNMs as the corresponding Kerr BH in GR,  $\omega_{lmn}^{\text{Kerr, scalar}}$ . However, our equation is nonhomogeneous as we also have the Gauss-Bonnet scalar evaluated on the background GR metric, acting as a source term. Particular solutions to the scalar equation introduce additional frequencies into the ringdown QNM spectrum [50, 103]. The spectrum of these “driven” modes by the source term for  $l \geq 2$  has been shown to coincide with the quasinormal modes for tensor perturbations for Kerr,  $\omega_{lmn}^{\text{Kerr, grav}}$ ;

while for  $l = 1$  the driven mode has been fitted empirically [50].

Can our scalar ringdown waveforms be modeled by the gravitational and/or scalar QNMs of a Kerr black hole in GR as above findings suggest? To address this question we perform one-mode ( $N = 1$ ) and two-mode ( $N = 2$ )

<sup>5</sup>However, there has been recent work on extending the Teukolsky formalism to modified gravity theories to compute their quasinormal modes for fast-rotating black hole solutions [102].

fits, whilst keeping the QNMs fixed to their values in GR. These fixed values employed in our analysis can be found in Table VI of Appendix C. For one-mode fits, we utilize Eq. (40), where we check whether just one QNM fixed to either  $\omega_{lmn}^{\text{Kerr, scalar}}$  or  $\omega_{lmn}^{\text{Kerr, grav}}$  describes the data well. Next, we perform a two-mode fit using Eq. (41), where we fix  $\omega_{lmn}^{\text{Kerr, scalar}}$  and  $\omega_{lmn}^{\text{Kerr, grav}}$  simultaneously. We note that for the  $l = 1$  ringdown modes fitted with the  $N = 2$  mode fit we take a conservative approach and only use a fundamental scalar QNM and its first overtone:

$$\text{Re}(\varphi_{N=1}^{lm}) = \begin{cases} A_1^{lm0} e^{-(t-t_0)/\tau_{lm0}} \cos(\omega_{lm0}(t-t_0) + p_1^{lm0}), & \omega_{\text{QNM}} \in \{\omega_{\text{QNM}}^{\text{Kerr, scalar}}, \omega_{\text{QNM}}^{\text{Kerr, grav}}\} \quad l, m > 1 \\ A_1^{lm0} e^{-(t-t_0)/\tau_{lm0}^{\text{Kerr, scalar}}} \cos(\omega_{lm0}^{\text{Kerr, scalar}}(t-t_0) + p_1^{lm0}) & l = m = 1, \end{cases} \quad (40)$$

$$\text{Re}(\varphi_{N=2}^{lm}) = \begin{cases} A_1^{lm0} e^{-(t-t_0)/\tau_{lm0}^{\text{Kerr, scalar}}} \cos(\omega_{lm0}^{\text{Kerr, scalar}}(t-t_0) + p_1^{lm0}) \\ \quad + A_2^{lm0} e^{-(t-t_0)/\tau_{lm0}^{\text{Kerr, grav}}} \cos(\omega_{lm0}^{\text{Kerr, grav}}(t-t_0) + p_2^{lm0}) & l, m > 1 \\ A_1^{lm0} e^{-(t-t_0)/\tau_{lm0}^{\text{Kerr, scalar}}} \cos(\omega_{lm0}^{\text{Kerr, scalar}}(t-t_0) + p_1^{lm0}) + \\ \quad A_2^{lm0} e^{-(t-t_0)/\tau_{lm1}^{\text{Kerr, scalar}}} \cos(\omega_{lm1}^{\text{Kerr, scalar}}(t-t_0) + p_2^{lm1}) & l = m = 1. \end{cases} \quad (41)$$

Equations (40) and (41) fit to the real parts of the scalar multipoles, as their imaginary parts will have the same amplitudes and phases. We make use of all scalar mode waveforms presented in Sec. III D, and therefore perform the fitting on the  $(lm) = (11), (22), (33), (44)$  modes.

We sample the parameter space using `emcee` [104]. Dropping the  $(lmn)$  indices in Eqs. (40) and (41) and keeping just the mode number  $N \in [1, 2]$ , we use uniform priors in our inference, namely  $\log A_i \in [-3, 1]$  and  $p_i \in [0, 2\pi]$  for  $i \in [1, N]$ . We compute the frequencies  $\omega_{lmn}$  with the `qnm` package [105] using our final spin calculations from Table II.

There is an ongoing debate around when the optimal time is to begin fitting quasinormal ringdown (see *e.g.* [106]), as different start times can give different answers for the mode fits, and have also caused some controversy regarding the confidence of a subdominant QNM observation in GW data [107]. While overtones are typically quick to decay, they can play an important role as we approach the time of merger [108–113]. To avoid the intricacies of having to account for overtones, as well as nonlinear effects in the early ringdown [114, 115], we take a conservative approach and start the ringdown analysis  $t_0 = 16M$  after the time of the peak amplitude of the scalar mode<sup>6</sup>. By starting too early we risk including nonlinear effects from the merger and by starting too late the SNR of the signal may significantly be lower. In our analysis, the damped sinusoid model is most accurate as an approximation in the late ringdown and so we sacrifice on the strength of the signal. The end time of our analysis is determined by the point in the late ringdown when the signal becomes very faint and the numerical noise becomes more significant. The point when this happens varies on the mode-by-mode basis, with higher modes being prone to numerical noise earlier than others. However, the typical length of our ringdown varies in the range of  $\sim 15 - 30M$ .

In the optimization process, we use a least-squares likelihood in the time domain, with a flat noise spectral density

$$L(d; \boldsymbol{\theta}) \propto \sum_i \exp\left(-\frac{(\varphi_{\bar{\theta}}(t_i) - d(t_i))^2}{2\sigma^2}\right), \quad (42)$$

where  $d(t_i)$  is the time sequence of numerical data,  $\sigma^2$  is the variance and  $\boldsymbol{\theta} = \{A_i, p_i\}$ . We estimate the variance by taking our total error budget percentage (*i.e.* 4%) from the peak of the amplitude for each mode. As such, the error we account for through the variance parameter varies on a mode by mode basis. This choice for error estimation in our analysis assumes that the total NR error is not correlated in time. In reality, this is not likely

to be an accurate assumption to make as in certain regions of the waveform we may in fact be overestimating or underestimating the allowed deviation of the data from the true values. Ideally, our likelihood function should contain some sort of correction to account for such correlation of the data with time. However, this is out of the scope of this work and we leave this for future study. We have verified the robustness of our choice of variance in the likelihood function of Eq. (42) by gradually decreasing its value and assessing its effect on the estimation of the modes' amplitudes. As expected, with decreasing variance, the amplitudes converge to some fixed values with smaller error bars, representing an ideal scenario where our NR error is very small. These idealized values provide the relative error we make in our fitting procedure when estimating amplitudes using our actual total NR error budget percentage to calculate fixed variance. Figure 7 shows this convergence of  $A_i$  for  $i \in [1, 2]$  of the (22) mode of the BBH-12 configuration, where the fixed variance of  $\sigma^2 = 0.003$  used in the fitting procedure results in median amplitudes lying within the error bars of the smallest variance.

In Table III we summarize the results of our fits. We note that we fixed the dimensionless coupling  $\beta_0/m_1^2$  to unity for convenience there. Therefore, when choosing a different value for the coupling, appropriate rescaling to the amplitudes has to be done according to Eq. (20). We find that the ratio of amplitudes of scalar Kerr QNMs to gravitational Kerr QNMs varies on a mode-by-mode basis for  $l > 1$  modes. In the case of the  $l = 1$  mode fit, the amplitude of the overtone  $n = 1$  dominates the amplitude of its fundamental mode as also found in the analysis of gravitational ringdown of Ref. [109]. Unless indicated by dots in Table III, we find that for certain modes a  $N = 1$  mode fit is able to describe the data accurately enough. This happens in the cases where the amplitude of one of the modes in the  $N = 2$  mode fit is dominant, or when the frequencies of the  $N = 2$  mode fit lie close to each other.

We additionally fit the amplitudes of our gravitational waveforms in Table IV, where we use  $(lm) = (11), (22), (33), (44), (55), (66)$  modes in the fitting procedure. We find that the  $N = 1$  mode fit of Eq. (37) is sufficient to describe the data. Since the Einstein equations to leading order remain unchanged (see Eq. (17)), we have fixed the frequency of the  $N = 1$  mode fit to the fundamental gravitational Kerr QNM of GR.

In summary, the leading order QNMs of the scalar and tensor components of the ringdown waveform in EsGB gravity are accurately described by QNMs of GR. The next correction in  $\epsilon$  to the scalar QNM spectrum would depend on the nature of the coupling to the Gauss-Bonnet term, while the correction to gravitational QNM spectrum would happen at  $\mathcal{O}(\epsilon^2)$ . In the case of subleading corrections to the scalar QNMs, for EdGB gravity with exponential coupling,  $\beta(\varphi) = e^\varphi$ , the next correction will come from second order in  $\epsilon$ , while for shift-symmetric Gauss-Bonnet gravity with coupling  $\beta(\varphi) =$

<sup>6</sup>We have investigated the choice of other start times ranging from  $10M$  to  $16M$  and found similar results on the estimated parameters.

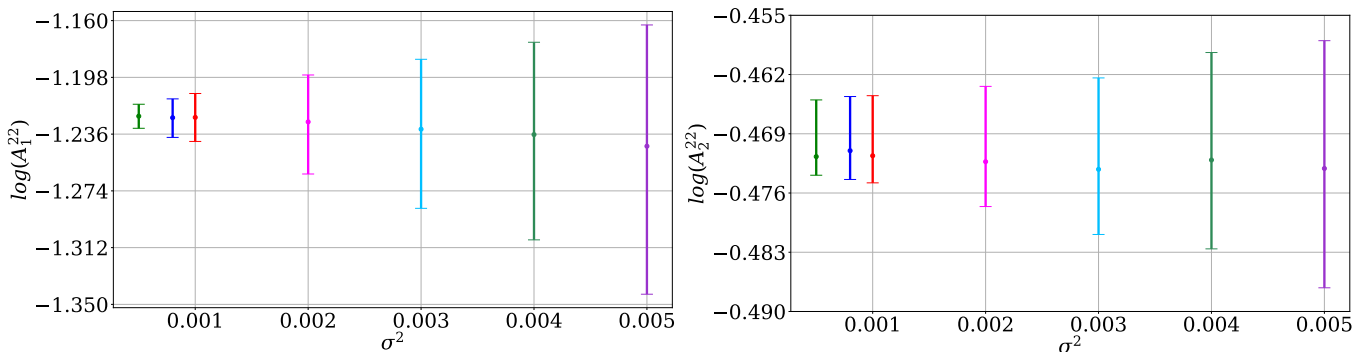


FIG. 7: Convergence of the estimated amplitudes with decreasing variance  $\sigma^2 = \{0.005, 0.004, 0.003, 0.002, 0.001, 0.0008, 0.0005\}$  of Eq. (42) for the (22) mode of BBH-12 run. The variance value estimated as 4% from the peak amplitude takes the value of  $\sigma^2 = 0.003$  in our fit for this configuration. We have verified that the same convergence holds qualitatively for the  $N = 1$  mode fit too.

$\varphi$ , at the third order in  $\epsilon$  [54]. Given the smallness of  $\epsilon$ , we expect any kind of deviation from GR in the scalar QNM spectrum in Gauss-Bonnet gravity to be very small.

## V. OBSERVATIONAL PROSPECTS

### A. Measurability of the scalar ringdown

Having formulated a model for the scalar polarization component of the EsGB ringdown waveform, we now make a first attempt to assess the measurability of its presence in compact binary coalescence observations by the current and future networks of GW detectors. Returning to Eq. (8), we recall that the second term predicts an additional scalar contribution, whose strength is controlled by the magnitude of the conformal coupling  $a_0$  defined in Sec. II B and the amplitude of the scalar field  $\varphi$ , which may be rescaled using the dimensionless parameter  $\beta_0/m_1^2$  according to Eq. (20). Therefore, the choice of the rescaling applied to the amplitude of the scalar field will affect the strength of the scalar polarization, and our choices of the re-scaling will be detailed in the following sections. However, before making predictions on the strength of the scalar signal, it is necessary to make the conversion to physical units. The scalar polarization now takes the form of

$$h_S = \frac{M_{\text{fin}}}{D_L} a_0 \varphi, \quad (43)$$

where  $M_{\text{fin}}$  is the final BH mass and  $D_L$  is its luminosity distance from the Earth. We note that  $\varphi$  is the sum of all ( $lm$ ) modes and is dependent on the inclination angle  $\iota$ , which is defined as the angle between orbital angular momentum and the line-of-sight

$$\varphi = \sum_{lm} \varphi^{lm} Y_{lm}(\iota). \quad (44)$$

In our analysis we set  $\iota = 60^\circ$ . As we discussed in Sec. II B, each polarization has a distinct geometrical im-

print on a GW detector. We therefore begin with projecting the scalar strain,  $h_S$ , onto the detector  $D$  located at  $\mathbf{x}_D$

$$h_D(t) = h_S(t, \mathbf{x}_D) F^S. \quad (45)$$

Here  $F^S$  is the response, or antenna pattern, of a detector  $D$  to scalar polarization. It can be given in terms of the polar angle  $\theta$  and the azimuthal angle  $\phi$  in the detector frame (*i.e.*  $\theta$  and  $\phi$  measured with respect to detector arms along the  $x$  and  $y$  axes) in the following form

$$F^S(\theta, \phi) = -\frac{1}{2} \sin^2 \theta \cos 2\phi. \quad (46)$$

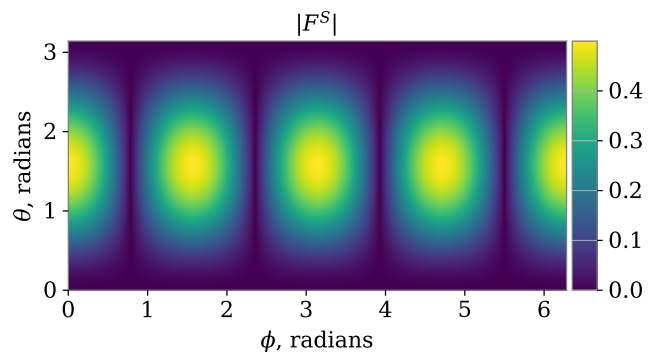


FIG. 8: Scalar antenna pattern for various choices of polar and azimuthal angles. Yellow regions indicate the maximum response from the detector from the incoming scalar-polarized GW.

Note the absence of dependence on the polarization angle  $\psi$  that defines the orientation of the source projected on the celestial sphere; this is a direct consequence of the spin-0 nature of the scalar field, in contrast with the tensorial GWs that behave as a spin-2 field. The response to scalar polarization depends on the polar and azimuthal

Run	$(lm)$ mode	$N = 2$		$N = 1, \omega_{lm}^{\text{Kerr,grav}}$ fixed	$N = 1, \omega_{lm}^{\text{Kerr,scalar}}$ fixed
		$\log_{10} A_1$	$\log_{10} A_2$	$\log_{10} A_1$	$\log_{10} A_1$
BBH-11	22	$-0.81^{+0.26}_{-0.02}$	$-0.67^{+0.01}_{-0.09}$	...	...
	44	$-1.62^{+0.04}_{-0.48}$	$-2.41^{+0.77}_{-0.39}$	...	$-1.58^{+0.01}_{-0.34}$
BBH-23	11	$-0.50^{+0.01}_{-0.02}$	$0.07^{+0.08}_{-0.04}$	...	...
	22	$-0.89^{+0.03}_{-0.03}$	$-0.61^{+0.01}_{-0.02}$	...	...
	33	$-1.34^{+0.03}_{-0.09}$	$-1.39^{+0.03}_{-0.07}$	...	...
	44	$-1.76^{+0.04}_{-0.16}$	$-2.59^{+0.46}_{-0.28}$	...	$-1.72^{+0.01}_{-0.58}$
BBH-12	11	$-0.10^{+0.01}_{-0.01}$	$0.69^{+0.18}_{-0.12}$	...	...
	22	$-1.23^{+0.05}_{-0.05}$	$-0.47^{+0.01}_{-0.01}$	$-0.48^{+0.01}_{-0.01}$	...
	33	$-1.30^{+0.17}_{-0.05}$	$-1.29^{+0.04}_{-0.07}$	$-1.09^{+0.01}_{-0.13}$	$-1.03^{+0.01}_{-0.01}$
	44	$-1.90^{+0.46}_{-0.12}$	$-1.40^{+0.03}_{-0.11}$	$-1.40^{+0.01}_{-0.32}$	...

TABLE III: Estimated amplitudes from the  $N = 1$  mode and  $N = 2$  mode fits summarized by Eqs. (40) and (41). As in Fig. 3, we set  $\beta_0/m_1^2 = 1$  for convenience. The dots indicate that a specific fit could not describe the data accurately. In all cases with an  $N = 2$  mode fit,  $A_1$  represents the amplitude of the scalar Kerr QNM. For (11) mode,  $A_2$  is the amplitude of the scalar Kerr overtone, while for all other modes,  $A_2$  represents the amplitude of gravitational Kerr QNM. The upper and lower limits on the estimated parameters lie within 90% confidence interval and the central value is the median.

Run	$(lm)$ mode	$\log_{10} A_1$
BBH-11	22	$-0.81^{+0.01}_{-0.01}$
	44	$-1.62^{+0.01}_{-0.01}$
	66	$-2.36^{+0.01}_{-0.01}$
BBH-23	22	$-1.04^{+0.01}_{-0.01}$
	33	$-1.58^{+0.003}_{-0.003}$
	44	$-1.75^{+0.01}_{-0.01}$
	55	$-1.93^{+0.01}_{-0.25}$
	66	$-2.51^{+0.01}_{-0.02}$
BBH-12	22	$-1.03^{+0.01}_{-0.01}$
	33	$-1.34^{+0.01}_{-0.01}$
	44	$-1.74^{+0.002}_{-0.001}$
	55	$-1.91^{+0.01}_{-0.01}$
	66	$-2.29^{+0.02}_{-0.03}$

TABLE IV: Estimated gravitational amplitudes of the  $N = 1$  mode fit of Eq. (37), where the fundamental gravitational QNMs are kept fixed. The upper and lower limits on the estimated parameters lie within 90% confidence interval.

angles at which the GW comes in with respect to the detector frame. Figure 8 illustrates the change of the antenna pattern for various angles. We position the source at an optimal sky location for one of the detectors (LIGO Hanford in particular), which is straight down one of its arms, *i.e.*  $\theta = \frac{\pi}{2}$ ,  $\phi = 0$ . We then compute the squared SNR of the scalar signal defined via

$$\rho^2 = \int_0^\infty \frac{4|\tilde{h}_D(f)|^2}{S_n(f)} df, \quad (47)$$

where  $\tilde{h}_D$  is the signal in the Fourier domain and  $S_n(f)$  is the noise power spectral density (PSD) of the detector, which we set to the estimated noise curve of i. the current network of LIGO (Hanford and Livingston) and

Virgo detectors at design sensitivity [116, 117] and ii. the Einstein Telescope (ET) [118] in the ET-D configuration [119]. We list luminosity distance and the range of masses chosen for each of the detectors in Table V.

Detector	$D_L/\text{Gpc}$	$M_{\text{fn}}/M_\odot$
LIGO/Virgo	1	[100, 1000]
ET	1	[10, 1000]

TABLE V: Distance and final BH mass range targeted with each of the detectors considered in this study.

In the computation of SNR from Eq. (47), the signal is weighted by the noise PSD curve in the frequency domain. Having a frequency of the scalar waveform close to the minima of the PSD would therefore increase the integrand of SNR for a fixed amplitude of the waveform. However, for varying mass, the amplitude is not fixed but scales according to Eq. (43). Further, the amplitude of the scalar signal is affected by the mass ratio: as suggested by our NR simulations from Sec. III D, amplitude increases for more asymmetric binaries.

We now move on to estimate the actual signal strength for two different scenarios with respect to the values of coupling parameters in EsGB.

### 1. Maximally allowed couplings

Our prior for the range allowed for the couplings  $a_0$  and  $\beta_0/m_1^2$ , is controlled by the theoretical and observational constraints described in Sec. II D. In this section we make the conservative choice of  $\max(\beta_0/m_1^2) = \epsilon_{\text{thr}} \approx 0.2$  and  $a_0^{\text{max}} = \sqrt{10^{-3}} \approx 0.0316$  to be maximally allowed values for our couplings (*i.e.* the blue region of Fig. 2 is where

the theory can be said to be no longer predictive) and investigate in more detail the dependence of the SNR of the scalar ringdown signal on the total mass  $M_{\text{fin}}$  and mass ratio  $q$  of the progenitors. Following common practice [120, 121], we assume  $\text{SNR} \geq 8$  is required for a detection.

Figure 9 shows the network SNR for the current LIGO (Livingston and Hanford) and Virgo detector network, calculated via quadrature,  $\rho_{\text{network}} = \sqrt{\sum_j \rho_j^2}$ , where  $\rho_j$  represents the SNR in a single detector. Here the values of numerically calculated SNR span three horizontal lines of constant  $q = \{1/2, 2/3, 1\}$  and are interpolated on the parameter space of  $M_{\text{fin}} \times q$ . The typical scalar signal is weaker than its tensorial counterpart by at least 3 orders of magnitude, and the choice of maximally allowed couplings results in increased SNR for larger masses. The largest network SNR of 1.8 is produced from the smallest mass ratio of  $q = 1/2$  and the final BH mass of  $M_{\text{fin}} = 1000M_{\odot}$ . We note, however, that our choice of  $t_0 = 16M$  to be the ringdown start time reduces the strength of the signal. As seen in Sec. IV, the amplitudes for highly asymmetric mass ratios become significantly damped at later times. Therefore, one may expect larger SNR, if an earlier ringdown start time was chosen.

The strength of the signal significantly improves in the ET, which we illustrate in Fig. 10. Here we further disentangle contributions of each mode to the total SNR by plotting SNR for the strongest individual modes, *i.e.*  $(lm) = (11), (22), (33)$ . We observe that some cross terms between modes may contribute destructively in the integrand of SNR (see Eq. (47)) and as such, the total SNR is not simply a sum in quadrature of the individual modes' contributions. We find that the strongest total SNR calculated from all modes is recovered from the most extreme mass ratio considered in our simulations,  $q = 1/2$ . This is as expected since its modes' amplitudes are significantly larger than for milder mass ratios. Assuming luminosity distance of  $D_L = 1\text{Gpc}$  for BBH-12 configuration, the total SNR of the scalar ringdown is weak for BHs with masses  $M_{\text{fin}} \lesssim 50M_{\odot}$  and falls beyond the detectability threshold. However, taking parameters of GW151226 event with  $q \sim 1/2$ ,  $D_L = 440\text{Mpc}$  and  $M_{\text{fin}} \sim 20.8M_{\odot}$  [122], we find the SNR in ET to be around 7.15. Interestingly, the SNR of individual modes has a more complicated structure and there are several competing factors contributing to their strength. First, the final BH mass determines where the QNM frequencies lie in relation to the high-sensitivity region of the detector's noise curve. Second, the hierarchy and relative amplitudes of the scalar modes are determined by the mass ratio of the progenitor (*e.g.* with odd- $m$  modes vanishing for symmetric binaries). Third, higher modes are less long-lived for more extreme mass ratios, meaning that at later ringdown start times these modes become significantly damped. Finally, the inclination angle contributes an additional  $l$ -dependent geometric factor to the relative mode amplitudes as seen by the observer. As

such, in our simulated analysis, the SNR of the (22) mode is the strongest for  $q = 2/3$  and (11) and (33) modes are the strongest for the  $q = 1/2$  one.

## 2. Imposing the most pessimistic constraint, $\sqrt{\beta_0} = 1.18\text{ km}$

So far we explored the strength of the signal in the optimistic scenario, where the strength of the EsGB dimensionless parameter is set at the limit of the theoretical bound and appears to be strong enough for certain binary configurations. Constraints on the EsGB coupling  $\beta_0$  coming from data analyses of astrophysical observations (see Table I) further limit the range of the coupling and therefore are expected to significantly lower the strength of the scalar signal. We now follow the analysis of [56] on GW signals from the inspiral of BBH and BH-NS binaries and set the value of the EsGB coupling to their quoted 90% combined upper bound, *i.e.*  $\sqrt{\beta_0} = 1.18\text{ km}$ . This result is based on an analytically approximated inspiral model, where the leading-order correction to the waveform at  $-1\text{PN}$  (*i.e.*  $\delta\Psi \propto (\beta_0^2/M^4)v^{-7}$ ) is inferred and mapped to a bound on  $\beta_0$ . Higher-order corrections to an incomplete 2PN level can vary the resulting bounds by more than 10%, depending on the binary parameters, therefore this value should not be considered as a robust upper bound at 90% confidence. Nevertheless, we expect that the upcoming fourth observing run (O4) of the LVK collaboration [117] will probe this value range with much higher confidence.

In this scenario the SNR of the scalar ringdown becomes significantly suppressed, which we demonstrate in Fig. 11 on a logarithmic scale. Unlike the previous case, where we bounded  $a_0$  and  $\beta_0/m_1^2$ , here, smaller values of the final BH mass and more asymmetric mass ratios yield a stronger scalar polarization signal, as expected. In particular, the largest SNR of 0.42 is observed for a binary of mass ratio  $q = 1/2$  with the smallest final mass of  $M_{\text{fin}} = 10M_{\odot}$ . Unless the source is observed at very small luminosity distance of  $D_L \sim 52.5\text{Mpc}$ , the scalar ringdown signal of this binary configuration will not be detectable even with third generation detectors. Our predictions are less pessimistic for lower-mass binaries at even higher mass ratios, however, in this work we do not consider BH-NS binaries or BHs with masses lower than  $5M_{\odot}$ .

## VI. BAYESIAN INFERENCE ON THE SCALAR RINGDOWN SIGNAL

We now perform full Bayesian inference on a hypothetical scalar signal present in the bands of the LVK detector network and ET. We model the data stream in each detector as

$$d(t) = h(t) + n(t), \quad (48)$$

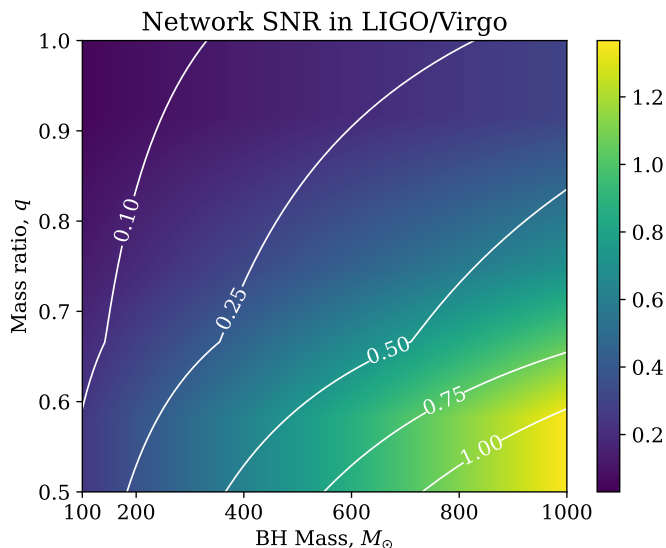


FIG. 9: Contour plot of network SNR in the  $M_{\text{fin}} \times q$  plane for the scalar ringdown of a BBH at 1 Gpc as observed by the Virgo, Livingston and Hanford network of detectors at design sensitivity. Here the couplings  $a_0, \beta_0/m_1^2$  are fixed to their maximally allowed values as described in Sec. V A 1. NR data are available along horizontal lines of  $q = \{1/2, 2/3, 1\}$ , based on which SNR values are estimated by interpolation on the plane.

where  $h(t)$  is the signal as described in Sec. IV and  $n(t)$  is a realization of detector noise. Although we use continuum-appropriate notation, in practice the above are realized as discrete time series with a sampling rate of 4096 Hz, which is sufficient for our purposes in this work.

### A. Analysis setup

Before delving into the details of our analysis, let us first describe the simplifications performed here. First, we assume that the GR part of the signal is well modeled and has been successfully reconstructed and removed from the data, without being particularly interested in the details of that part of the analysis. In practice this means that we have reduced the problem of performing an apples-to-apples comparison between GR and EsGB to the problem of searching for the presence of our EsGB scalar-ringdown signal in the residual data. This, in turn, makes use of the decoupling-limit assumption, that is, GW generation is driven by GR dynamics and therefore the tensorial ringdown signals in GR and EsGB are identical. Furthermore, we factorize the analysis of multiple QNMs into individual analyses for each  $(lm)$  pair, here performed using  $N = 1$  or  $N = 2$  modes for each pair that can capture the presence of a “gravity-led” mode (or even an unusually strong overtone). This simplification assumes that the frequency content of *e.g.* the  $l = m = 1$  and  $l = m = 2$  modes that are studied here can be separated into disjoint regions in the frequency domain, as was done in recent searches for subdominant modes [107]. Although this latter assumption may not always hold,

prior information on the final BH parameters, and hence on the expected scalar spectrum, will always be available from the analysis of the much louder tensorial signal (“+” and “ $\times$ ” polarizations), thus allowing for the scalar analysis setup to be adapted accordingly. Details related to the above considerations will not be discussed here, but are left to be explored in future work.

We thus define our two competing hypotheses as follows:

1.  $\mathcal{H}_0$  is our null hypothesis, corresponding to the data consisting of pure Gaussian noise, according to the PSD of each detector in our network.
2.  $\mathcal{H}_1$  is our scalar-ringdown signal hypothesis, corresponding to the presence of a scalar signal in addition to noise in our data, where the scalar model is described in Sec. IV and is parametrized by the real QNM amplitudes and phases  $(A_k^{lm}, p_k^{lm})$ , while the complex mode frequencies are fixed to their expected values (see details in Eqs. (40) and (41)).

Our first task is then to infer whether our hypothetical scalar signal could be identified as being present in the data—according to (48), where  $h(t) = h_S(t; \vec{\theta})$  is consistent with our scalar signal model—or the data is consistent with pure noise *i.e.*  $h(t) = 0$ . For scalar signals that are detected with confidence against the noise hypothesis, our analysis will also estimate the parameters  $\vec{\theta}$  of our scalar ringdown model as posterior probability distributions on the model parameter space  $p(\vec{\theta}|d, \mathcal{H}_1)$ . To accomplish this, we inject our NR scalar waveforms  $h_S(t)$  into data streams of simulated Gaussian noise and perform time-domain ringdown analysis using



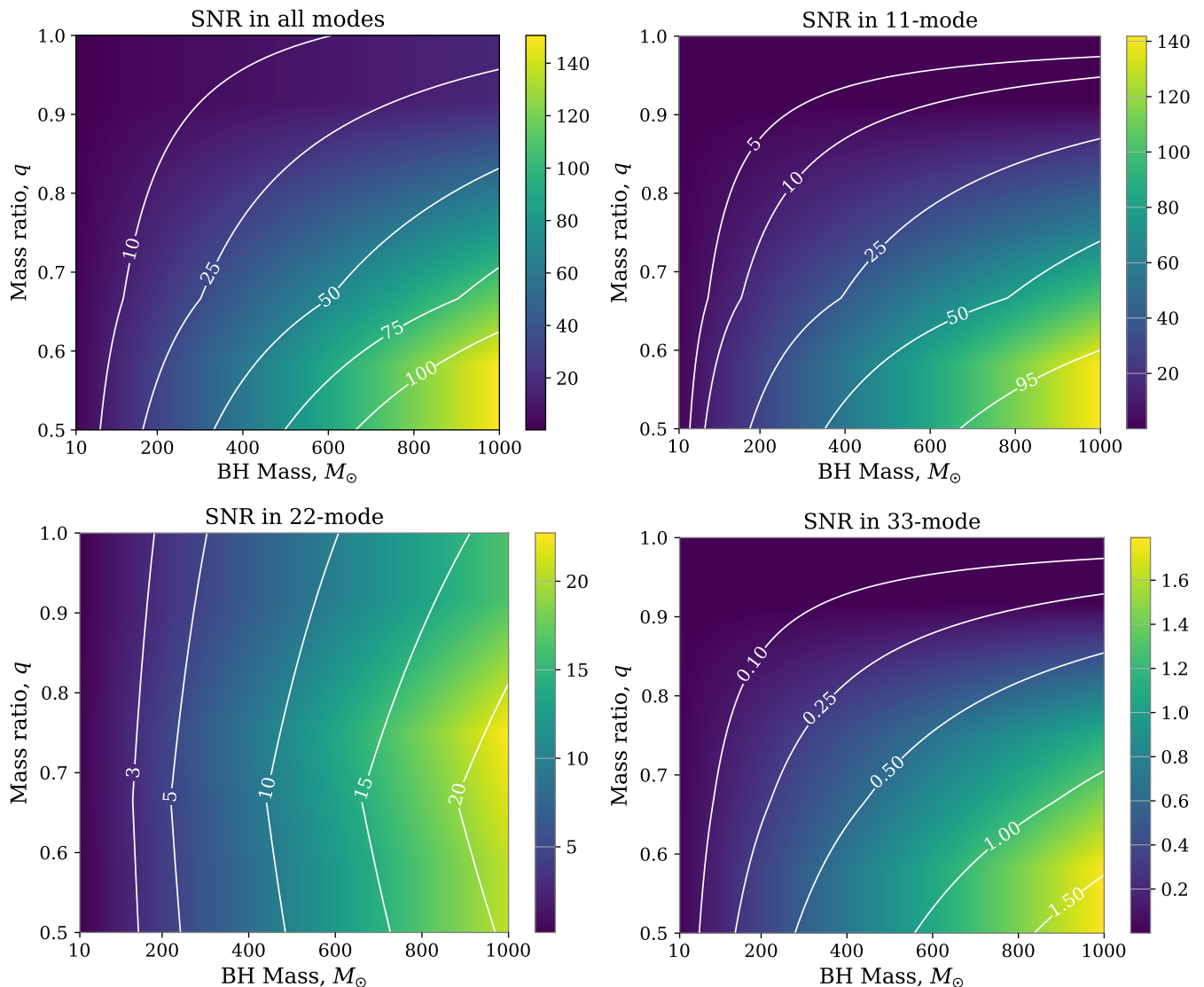


FIG. 10: Contour plot of network SNR in the  $M_{\text{fin}} \times q$  plane for the scalar ringdown of a BBH at 1 Gpc as observed by the Einstein Telescope. The couplings  $a_0, \beta_0/m_1^2$  are fixed to their maximally allowed values as described in Sec. V A 1. The top left panel shows the total SNR, while the individual scalar mode SNRs are shown in the remaining three panels. NR data are available along horizontal lines of  $q = \{1/2, 2/3, 1\}$ , based on which SNR values are estimated by interpolation on the plane.

the `pyRing` pipeline [123–125], which relies on a Python implementation of the nested sampling algorithm [126] called `CPNest` [127]. The built-in calculation of the evidences  $P(d|\mathcal{H}_i)$  in nested sampling, by statistically integrating each likelihood function  $p(d|\vec{\theta}_i, \mathcal{H}_i)$  over the respective parameter space  $\Sigma_i$ , enables model selection between the signal and noise hypotheses, by means of the Bayes factor,

$$\mathcal{B}_0^1 = \frac{P(d|\mathcal{H}_1)}{P(d|\mathcal{H}_0)} = \frac{\int_{\Sigma_1} p(d|\vec{\theta}_1, \mathcal{H}_1) p(\vec{\theta}_1|\mathcal{H}_1) d\vec{\theta}_1}{\int_{\Sigma_0} p(d|\vec{\theta}_0, \mathcal{H}_0) p(\vec{\theta}_0|\mathcal{H}_0) d\vec{\theta}_0}. \quad (49)$$

Since  $\mathcal{H}_0$  here is the noise hypothesis, its parameter space is the empty set and the integral in the denomina-

tor reduces to a product of noise likelihoods  $p(d|\mathcal{H}_0) \propto \exp\{-\frac{1}{2} \sum_{i,j} d_i C_{ij}^{-1} d_j\}$ , one for each detector, where  $C_{ij}$  is the two-point autocovariance matrix, which characterizes the detector noise in the time domain as a discrete stochastic process that is assumed to be Gaussian and stationary [124]. Similarly, the pointwise likelihood for  $\mathcal{H}_1$  is computed using the same expression, where we replace  $d \rightarrow d - h_S(t; \vec{\theta})$ . That is, the signal hypothesis states that the residual is pure noise.

We adopt two approaches in the injection of the scalar signal. First, we perform a zero-noise injection by setting  $n(t) = 0$  in (48), in order to isolate possible biases due to realization-specific effects of the noise in our analysis and



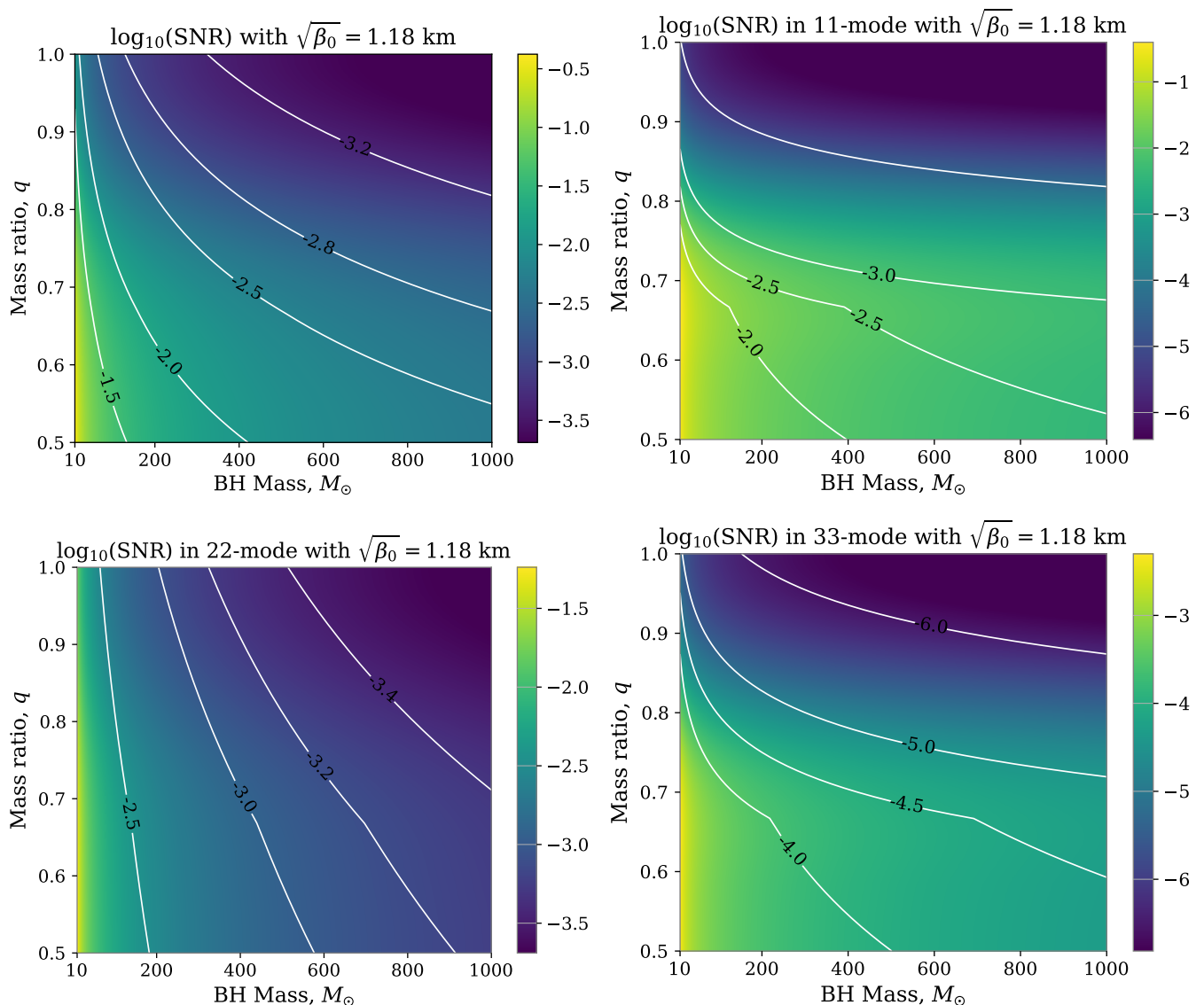


FIG. 11: Same as Fig. 10, except here the Gauss-Bonnet coupling  $\sqrt{\beta_0} = 1.18$  km is fixed and the plot is given on a logarithmic scale. For more discussion see Sec. V A 2.

disentangle them from potential systematic biases inherent to our model. Note, however, that since the likelihood is weighted by the noise PSDs of our GW detectors, the overall effect of the noise on the uncertainty of our measurements is still incorporated in our method. Second, we inject the scalar waveform into simulated noise and assess its effects on the parameter estimation. We have followed the standards of the LIGO Scientific Collaboration Algorithm Library (LAL) [128] to perform NR scalar waveform injections, for which we have used a modified version of `LALSuite` [129] to accommodate the construction of the scalar waveform.

We present results for the injection of the BBH-12 binary configuration, which gives us the strongest scalar wave signal. We place the source along one of the arms of the detector, as described in Sec. V A, at a luminos-

ity distance of  $D_L = 100$  Mpc, and choose a final mass of  $M_{\text{fin}} = 500M_\odot$ . We choose to inject the two loudest modes ( $lm = (11)$  and  $(lm) = (22)$ ) and further take maximally allowed values for the theory couplings  $\beta_0/m_1^2$  and  $a_0$  as described in Sec. V A, *i.e.*  $\max(\beta_0/m_1^2) = 0.2$  and  $a_0^{\text{max}} = \sqrt{10^{-3}} \approx 0.0316$ . The SNR value for the configuration involving the (11) mode is roughly 700 and for the (22) is around 100. We use Table III of Sec. IV to determine which recovery model of Eqs. (40) and (41) to use for each of our injections. As such, for the (11) mode, we use the  $N = 2$  fit with frequencies fixed to the fundamental and first overtone scalar Kerr QNMs, while for the (22) mode we use the  $N = 1$  mode fit with the frequency fixed to the fundamental gravitational Kerr QNM.

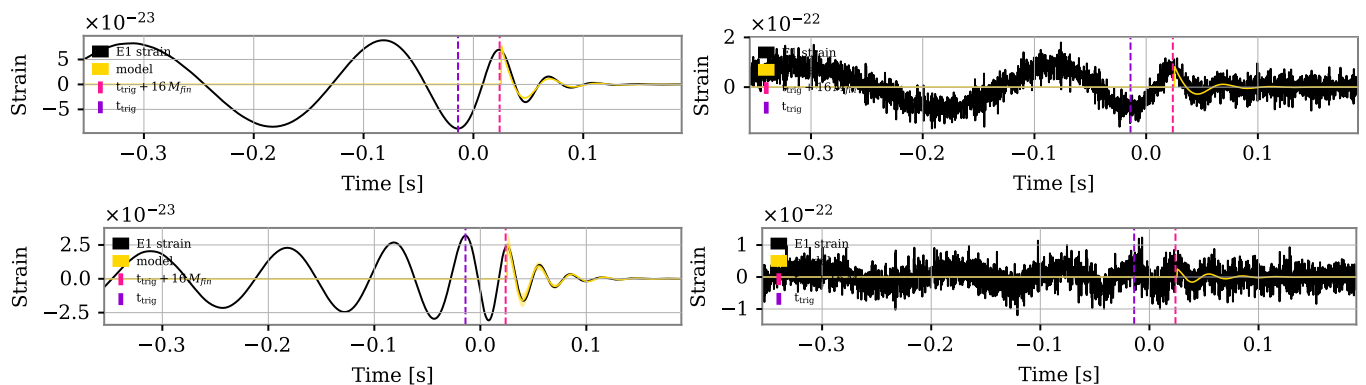


FIG. 12: Reconstructed waveforms for (11) (top) and (22) (bottom) modes for the scalar field for an injection into the Einstein Telescope. The left panel illustrates zero-noise injections and the right panel Gaussian-noise injections. The yellow line shows the recovered damped sinusoid model for each of the modes (see the main text for the details), the dashed purple and pink lines show the trigger time (defined as the reference time in the reference detector) and ringdown start time respectively. For more discussion see Sec. VI B.

## B. Results

Using the two hypotheses,  $\mathcal{H}_1$  and  $\mathcal{H}_2$ , as defined in Sec. VI A, in Fig. 12, we present the results of the recovery of the (11) and (22) modes with zero-noise and colored Gaussian noise injections in ET. The results suggest that the scalar-ringdown signal hypothesis  $\mathcal{H}_1$  is favored for both injections, *i.e.* the data contains a scalar-polarized GW present at the expected frequencies within the detector’s sensitivity band. The Bayes factors for the zero-noise and Gaussian noise injections are  $\ln \mathcal{B}_0^1 \sim 16771$  and  $\ln \mathcal{B}_0^1 \sim 16127$ , and  $\ln \mathcal{B}_0^1 \sim 47$  and  $\ln \mathcal{B}_0^1 \sim 15$  for the (11) and (22) modes, respectively. Finally, in Fig. 13, we demonstrate the effect of Gaussian noise on the estimation of the modes’ amplitudes and phases. Overall, with the source parameters of our choice we conclude that Gaussian noise does not compromise our ability to measure scalar polarization, neither does it introduce significant biases in recovering the modes.

As we have seen in Sec. V A, for a fixed set of coupling parameters  $a_0$  and  $\beta_0/m_1^2$ , larger total masses or more extreme mass ratios are needed to achieve higher SNRs at a given distance. From the observational point of view, the astrophysical population statistics for BBH systems allow for a rather faint probability of either placing stringent bounds on EsGB or making a direct detection, based on the scalar ringdown signal of a single BBH source, even with a 3G/XG detector. Having multiple detectors in the network and combining information from multiple BBH events across a wide mass range will improve our overall sensitivity to the consistent presence of such signals. As the rate of BBH events with  $\text{SNR} > 100$  in the next-generation network is expected to reach  $\mathcal{O}(10^2 - 10^3)$  per year [130], joint information from multiple events, even if they may be weak, will statistically improve the confidence of detecting a scalar signal as well as the precision of the inference by roughly a factor of  $\sim \sqrt{n}$ ,  $n$  being the number of detected scalar signals [131]. While the

presence of scalar polarization in the ringdown spectrum will be a smoking gun (unlike the inspiral dephasing), indicating the existence of a fundamental scalar field, more care will be needed in disentangling this weak effect from noise artifacts and other systematics.

## VII. CONCLUSION

Through the presence of a conformal coupling to matter, black hole binaries in EsGB gravity emit gravitational waves that have a scalar polarization. The family of theories we consider in this work is controlled by two coupling parameters: the Gauss-Bonnet coupling  $\beta_0$  and the conformal coupling  $a_0$ , which both impact the strength of the scalar-polarized gravitational wave. We have studied the extent to which these couplings could be constrained through gravitational wave observations of the scalar polarization during binary black hole ringdown. By exploring the parameter space in the range of validity of our couplings, and calculating respective signal-to-noise ratios, we conclude that the scalar polarization has a low chance of being detected. There is a stronger possibility of detection with next generation detectors like the Einstein Telescope, targeting larger masses or more asymmetric binary progenitors, given the observed amplification in the scalar polarization amplitude for those systems from our NR simulations. Furthermore, future observations with LISA [132] may possibly allow for more precise measurements of ringdown from extreme mass-ratio inspirals, although the much higher mass range that LISA will probe may not be favorable for sourcing sufficiently strong scalar modes in theories like the ones studied here. The SNR is greatly dependent on the value of the dimensionless EsGB parameter,  $\beta_0/m_1^2$ . Even at the largest allowed theoretical value for the dimensionless coupling ( $\beta_0/m_1^2 \sim 0.2$ ), one would need to have total mass of roughly  $\gtrsim 50M_\odot$

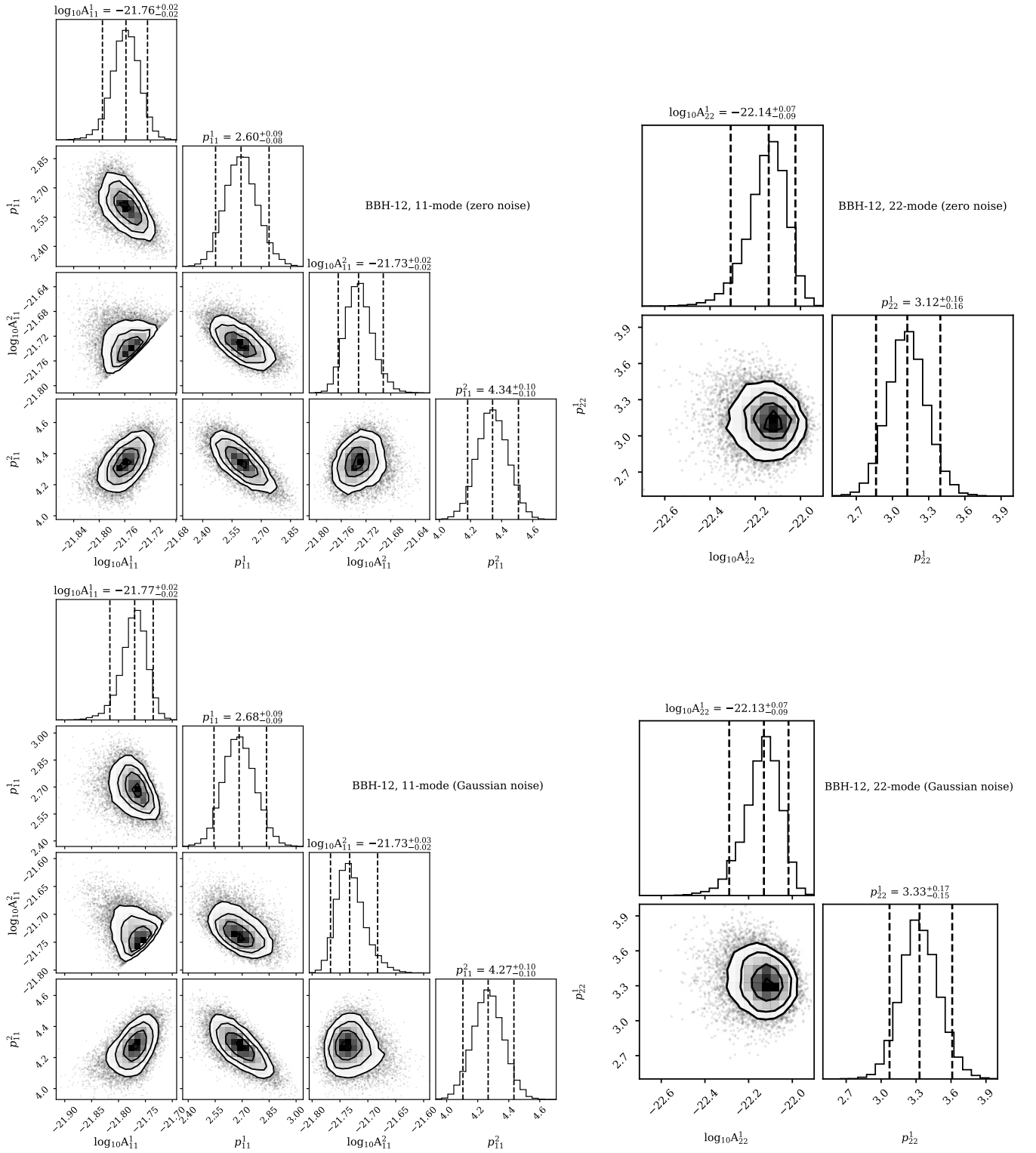


FIG. 13: Joint posterior distributions for the amplitudes and phases recovered for (11) and (22) modes. The upper panel shows the parameters for the zero-noise injections and the lower panel for the Gaussian noise injections. The upper and lower limits on the estimated parameters lie within 90% confidence interval. Parameter estimation from both injections clearly demonstrates that noise does not bias the recovered amplitudes and phases significantly. For more discussion see Sec. VI B.

and a fairly asymmetric mass ratio ( $q \sim 1/2$ ) in order for there to be a detection with a future generation GW

detector. For smaller values of  $\beta_0/m_1^2$ , the strength of the signal drops beyond the detectability threshold for any inspiral scenario we considered, even for the Einstein Telescope. Given the present observational constraint of  $\sqrt{\beta_0} \lesssim 1.18\text{km}$ , and that  $M_\odot \sim 1.5\text{km}$  in geometrized units, detecting a scalar polarization in a  $50M_\odot$  event requires the smaller mass black hole to have a mass of  $\sim 2.5M_\odot$  in order for a competitive constraint on  $\beta_0$  to be possible from a ringdown measurement with the Einstein Telescope.

The most stringent constraint on most modified theories of gravity comes from the inspiral, through measurements of the phase of the gravitational wave signal [14, 56]. This being said, a measurement of the inspiral phase does not completely determine the nature of a potential deviation from GR, as the dephasing could come from the emission of energy in other energy channels beyond (for example) that of a gravitational scalar field. Measuring the ringdown signal provides a complementary test to the measurement of the inspiral phase.

Apart from performing a targeted test on the GW data for signs of our EsGB model, the method that we propose here can be applied to a more general setting. EsGB with a conformal scalar coupling in its decoupling limit [133, 134] is a prime example of a well-motivated theory, in which the spin-0 QNMs of the Kerr metric are excited and observed via radiation of scalar GWs. Since backreaction can be neglected in the limit of a small coupling  $\beta_0/m_1^2$ , part of the scalar quasinormal mode spectrum is identical to that of the spectrum of a (massless) scalar about a Kerr black hole [50, 96]. More generally, any alternative theory featuring an additional scalar field that couples to the matter-field metric will also radiate spin-0 QNM frequencies, provided that the theory respects the “no-backreaction” property (*i.e.* to leading order, the GR sector determines the background metric and is driving the dynamics). In short, the general strategy amounts to using the information from the observed tensorial QNM frequencies to measure the remnant BH parameters, fixing the spin-0 QNM frequencies, and subsequently searching for the presence of any residual scalar GW signal on those frequencies, while being agnostic about the amplitude of each mode. The mode amplitudes are sensitive to the details of a given theory, since the field equations will determine how strongly each mode is sourced from the initial perturbation. Therefore, following the detection of a scalar signal, measurements of the relative mode amplitudes, combined with measurements on progenitor parameters, will narrow down the specifics of the theory and its couplings. A similar approach could also cover theories featuring a gravitational vector field. A thorough analysis of this strategy is beyond the scope of this article.

There are several more directions for future work. We have only considered the impact of the scalar polarization on the ringdown; it would be interesting to see if stronger constraints could be placed on  $\beta_0$  and  $a_0$  from polarization measurements of the inspiral waveform. We

have solved for the equations of motion of EsGB gravity in the decoupling limit. While this approximation has been shown to be accurate for modeling the scalar waveform in EsGB gravity, at least during the inspiral phase of evolution (and ignoring the effects of dephasing) [50], it would be interesting to compare it to full solutions to EsGB gravity [26, 27, 54]. It will also be important to extend our study to spinning progenitors and see whether the scalar mode amplitudes’ dependence on spins follows a functional form similar to that of the tensorial modes [135, 136]. Finally, while we have argued that EsGB gravity with a conformal scalar coupling to the metric may give the largest scalar polarization signal for black hole binaries among scalar-tensor gravity theories, it would be interesting to numerically model other modified theories of gravity featuring scalar or vector-polarized gravitational waves and devise similar targeted tests.

## ACKNOWLEDGMENTS

We thank Ulrich Sperhake and Daniela Doneva for useful conversations on aspects of this project, Miren Radia for the help with GRChombo, Danny Laghi and Gregorio Carullo for getting started with pyRing and Maxence Corman for reviewing our preprint. We also thank the entire GRChombo collaboration for their support and code development work.

T.E. is supported by the Centre for Doctoral Training (CDT) at the University of Cambridge funded through the STFC. M.A. is supported by the Kavli Foundation. J.L.R. acknowledges support from STFC Research Grant No. ST/V005669/1, and from the Simons Foundation through Award No. 896696.

This research project was conducted using computational resources at the Cambridge Service for Data Driven Discovery (CSD3) system at the University of Cambridge, provided by Dell EMC and Intel using Tier-2 funding from the Engineering and Physical Sciences Research Council (Capital Grant No. EP/T022159/1), and DiRAC funding from the Science and Technology Facilities Council ([www.dirac.ac.uk](http://www.dirac.ac.uk)), and Cosma7 of Durham University through Grants No. ST/P002293/1, No. ST/R002371/1 and No. ST/S002502/1, Durham University and STFC operations Grant No. ST/R000832/1. Some of the simulations presented in this article were also performed on computational resources managed and supported by Princeton Research Computing, a consortium of groups including the Princeton Institute for Computational Science and Engineering (PICSciE) and the Office of Information Technology’s High Performance Computing Center and Visualization Laboratory at Princeton University.

## Appendix A: Convergence testing and error estimation

### 1. Gravitational and scalar waveforms

In this section we follow the methodology of [72]. We start with our results on the convergence of the code and the discretization error due to finite resolution for simulation configuration BBH-11. We use  $\Delta x_{\text{high}} = 2M$ ,  $\Delta x_{\text{med}} = 2.67M$  and  $\Delta x_{\text{low}} = 3.2M$  on the coarsest level of high, medium and low resolution runs, respectively. We note that the results presented in the main body were obtained from evolving the higher resolution configuration. The order of convergence is estimated for the amplitude and phase of  $\Psi_4$ :

$$\Psi_{4,lm} = \Psi_{4,lm}^A e^{i\Psi_{4,lm}^\phi}. \quad (\text{A1})$$

In Fig. 14, where we have already multiplied the difference between medium and high resolutions by an appropriate factor, we plot the convergence order for the amplitude and phase of  $\Psi_4$ . The convergence factor of order  $n$  for a given quantity  $\tau$  is calculated by its difference at low/medium and medium/high resolutions:

$$Q_n = \frac{\tau_{\text{low}} - \tau_{\text{med}}}{\tau_{\text{med}} - \tau_{\text{high}}}. \quad (\text{A2})$$

In the continuum limit the truncation error typically approaches zero as a power of the discretization parameter  $\Delta x$ , that is for a given approximation error of order  $n$ ,

$$\lim_{\Delta x \rightarrow 0} \tau_{\Delta x} = \Delta x^n \times \text{const.} \quad (\text{A3})$$

Therefore, in the continuum limit the convergence factor reduces to

$$Q_n = \frac{\Delta x_{\text{low}}^n - \Delta x_{\text{med}}^n}{\Delta x_{\text{med}}^n - \Delta x_{\text{high}}^n}. \quad (\text{A4})$$

For the amplitude of  $\Psi_4$  we find the convergence order to be between second and third order in the inspiral, which then increases to between third and fourth in the late inspiral and merger. For the phase of  $\Psi_4$  we find convergence consistent with fourth order dropping to third around merger. We perform a similar analysis for the amplitude of the scalar field amplitude and find the order of convergence fluctuating between second and third as indicated in the left panel of Fig. 15.

To estimate the discretization error for the amplitude  $e_A$ , we measure the relative percentage error between the finest resolution result and Richardson extrapolation, while for the phase error  $e_\phi$  we simply give it as the difference,

$$e_A = \frac{|\Psi_{4,lm}^A - \Psi_{4,lm}^{A,\text{Richardson}}|}{\Psi_{4,lm}^{A,\text{Richardson}}} \times 100\%, \quad (\text{A5})$$

$$e_\phi = |\Psi_{4,lm}^\phi - \Psi_{4,lm}^{\phi,\text{Richardson}}|. \quad (\text{A6})$$

Finally, to estimate the error due to finite radius extraction we compute a given radiated quantity at several finite extraction radii and extrapolate to infinity by fitting a polynomial in  $1/r$ . We use first order extrapolation of polynomial order  $n = 1$ :

$$\Psi_{4,lm}^{i,n=1} = \frac{\Psi_{4,lm}^i}{r}. \quad (\text{A7})$$

We then compute the corresponding errors for the amplitude and phase as given in Eqs. (A5) and (A6), where Richardson extrapolated quantities are now replaced by the extrapolated quantities prescribed by Eq. (A7).

Additionally, we present convergence results for BBH-12 configuration, where we now use  $\Delta x_{\text{high}} = 2M$ ,  $\Delta x_{\text{med}} = 2.29M$  and  $\Delta x_{\text{low}} = 2.67M$  on the coarsest level of high, medium and low resolution runs respectively. We present our results in Fig. 16 and the right panel of Fig. 15 for the gravitational (22) mode of  $\Psi_4$  and the scalar field amplitude respectively. We find similar results to BBH-11 configuration. We observe between second and third orders of convergence in the amplitude and between third and fourth orders of convergence for the phase. The convergence order for the scalar field amplitude is second order in the inspiral and fourth order in the merger and ringdown.

### 2. GW energy and angular momentum flux convergence

Finally, we present convergence plots for BBH-11 of GW energy flux and GW angular momentum flux computed with the use of Eqs. (31) and (32), respectively. We employ the same set of resolutions as in Sec. A 1 and compute the total radiated energy and the total angular momentum flux, as described in Sec. III C of the main text.

From Fig. 17, we conclude that both the energy flux and angular momentum flux have an order of convergence between third and fourth. By using third order Richardson extrapolation, we estimate the error for final mass and spin to be of 0.01% and 0.05%, respectively.

## Appendix B: Code Validation

In this section we address the tests on the implemented Gauss-Bonnet term in `GRChombo`. First of all, we performed a self-convergence test by evolving a scalar field on a Schwarzschild background. We use  $\Delta x_{\text{high}} = 1.347M$ ,  $\Delta x_{\text{med}} = 1.6M$  and  $\Delta x_{\text{low}} = 2M$  on the coarsest level of high, medium and low resolution runs respectively. Fig. 18 demonstrates our results and overall we find second order of convergence.

Finally, we compare our numeric result for a scalar field evolved on a Schwarzschild background to the analytic solution in the Painlevé-Gullstrand (PG) coordinates. By

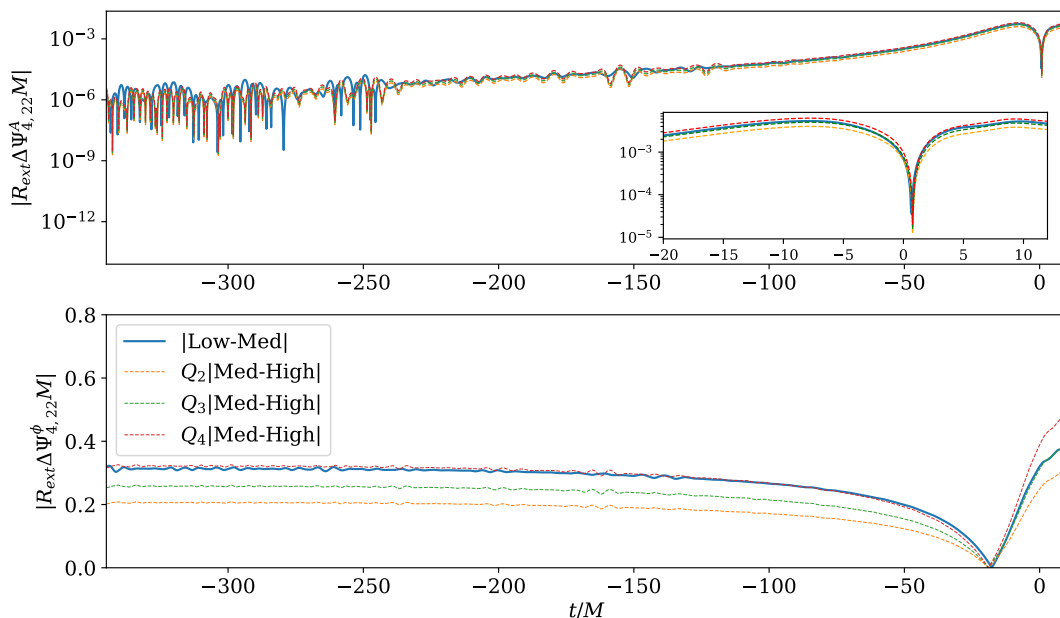


FIG. 14: Convergence of  $\Psi_{4,22}$  extracted at  $R_{\text{ex}} = 110M$  for BBH-11 configuration. *Top*: convergence of the amplitude,  $\Psi_{4,lm}^A$ . The difference for medium/high resolutions is rescaled according to second and third orders of convergence. The inset shows an interval around the merger. *Bottom*: convergence of the phase,  $\Psi_{4,lm}^\phi$ . The difference for medium/high resolutions is rescaled according to third and fourth orders of convergence.

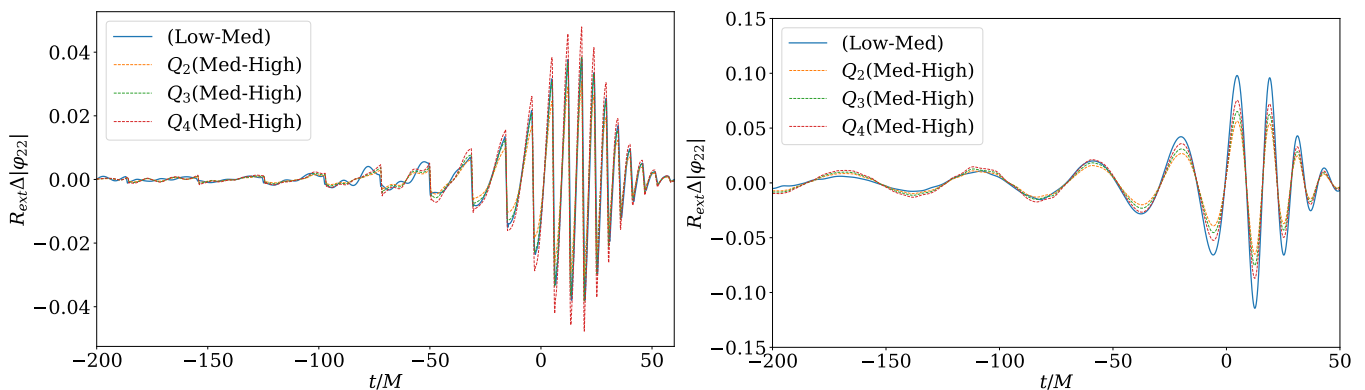


FIG. 15: *Left*: convergence of the amplitude of  $\varphi_{22}$  extracted at  $R_{\text{ex}} = 110M$  for BBH-11 configuration. The difference for medium/high resolutions is rescaled from second to fourth orders of convergence. *Right*: same as left but for BBH-12 configuration.

starting with the scalar field equation

$$\square\varphi + \beta_0\mathcal{R}_{GB} = 0, \quad (\text{B1})$$

we impose a regularity condition of  $\partial_r\phi$  at the horizon  $r = 2M$  and the falloff of the scalar field at infinity,  $\lim_{r \rightarrow \infty} \phi = 0$ . We find an analytic solution given in terms of PG coordinates by

$$\varphi(x) = \frac{2\beta_0}{M} \left( \frac{1}{x} + \frac{1}{x^2} + \frac{4}{3x^3} \right), \quad \text{where } x = \frac{r}{M}. \quad (\text{B2})$$

We then calculate the  $L1$ -norm for the analytic and numeric solutions and normalize it over the total volume.

Figure 19 shows good agreement between solutions after  $t \sim 100M$ , when the scalar has grown and settled to a constant value.

### Appendix C: Quasinormal modes of a Kerr black hole in GR

In Sec. IV and in particular Eqs. (40) and (41), we utilize QNMs of a Kerr black hole in GR to perform numerical fits to our data. In Table VI we present the values of the frequencies ( $\omega_{lmn}$ ) and damping times ( $\tau_{lmn}$ ),

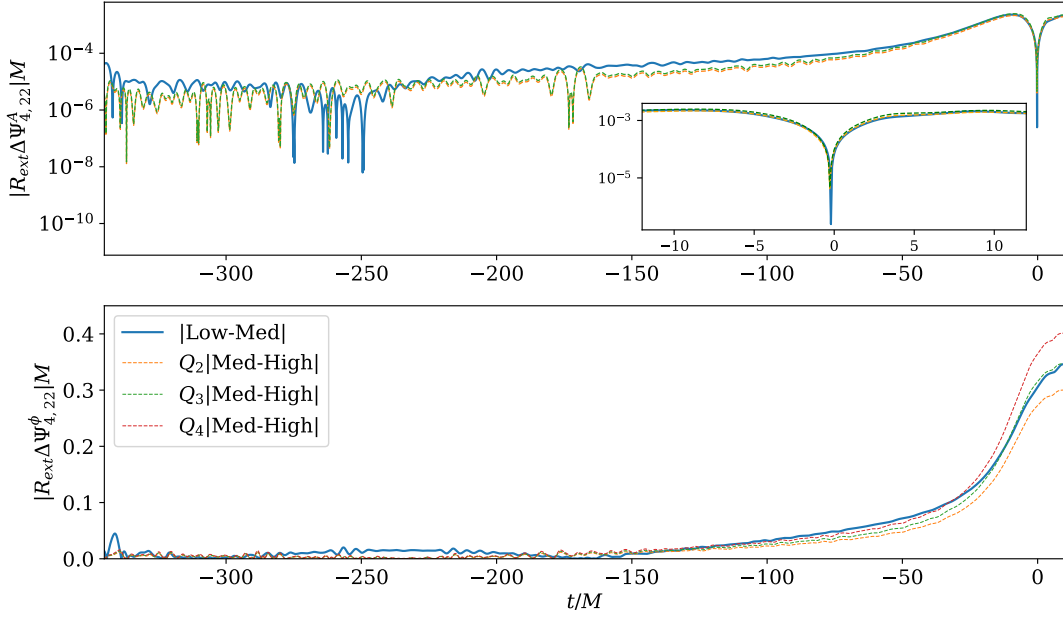


FIG. 16: convergence of  $\Psi_{4,22}$  extracted at  $R_{\text{ext}} = 110M$  for BBH-12 configuration. *Top*: convergence of the amplitude,  $\Psi_{4,lm}^A$ . *Bottom*: convergence of the phase,  $\Psi_{4,lm}^\phi$ .

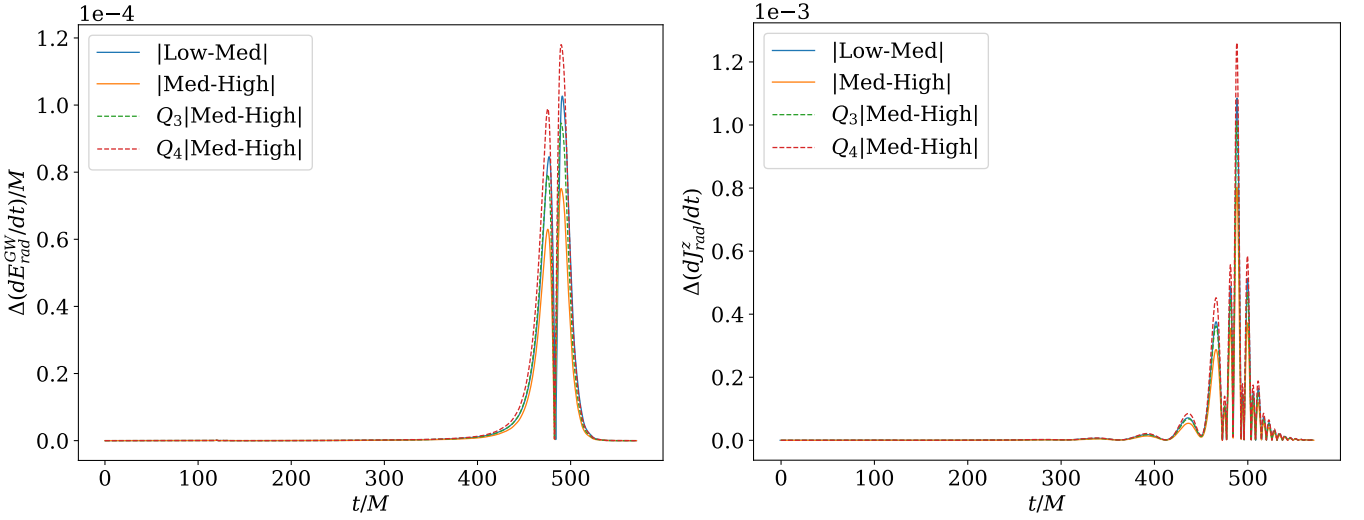


FIG. 17: *Left*: convergence of the energy flux extracted at  $R_{\text{ext}} = 110M$  for BBH-11. The difference for medium/high resolutions is rescaled according to third and fourth orders of convergence. *Right*: same as left but the diagnostic quantity is the angular momentum flux in the  $z$  direction extracted at  $R_{\text{ext}} = 110M$  for BBH-11.

of the gravitational quasinormal modes of the remnant black hole. These modes were computed using the `qnm` package [105].

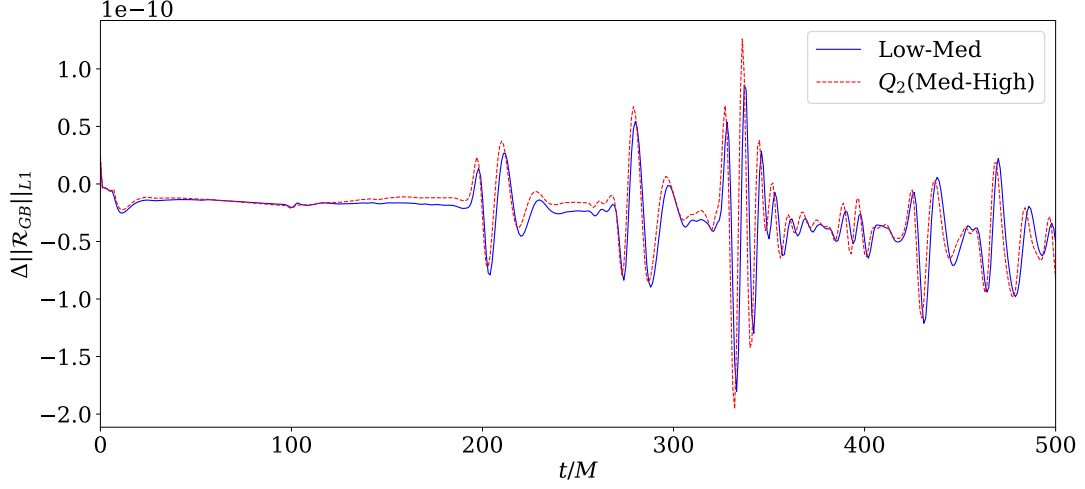


FIG. 18: Self-convergence of the  $L1$ -norm normalized over the total volume for the Gauss bonnet term. The difference for medium/high resolutions is rescaled according to the second order convergence.

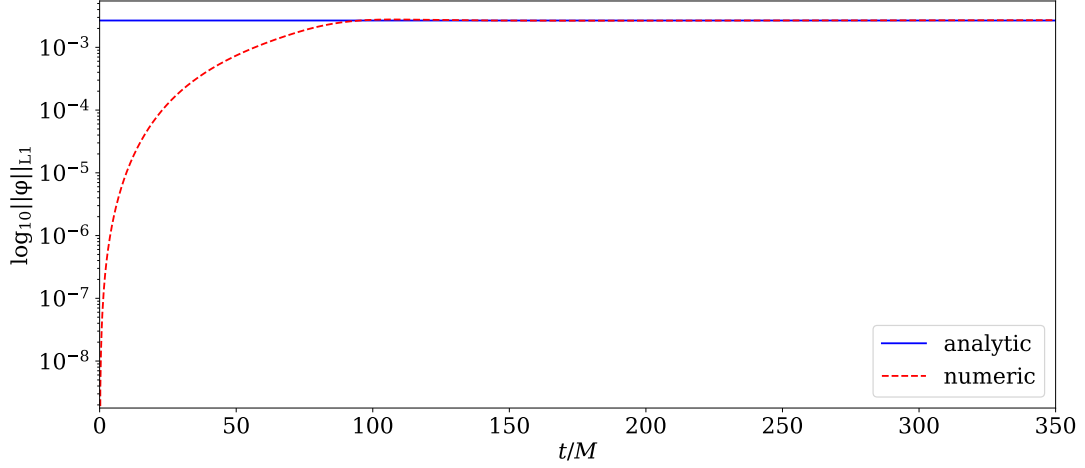


FIG. 19: Comparison of the  $L1$ -norm of the scalar field profile normalized over total volume for numeric and analytic solutions.

Run	$(lmn)$ mode	$\omega_{lmn}^{\text{Kerr,scalar}}$	$\tau_{lmn}^{\text{Kerr,scalar}}$	$\omega_{lmn}^{\text{Kerr,grav}}$	$\tau_{lmn}^{\text{Kerr,grav}}$
BBH-11	(220)	0.6526	11.3627	0.5291	12.3320
	(440)	1.2083	11.4250	1.1356	11.8200
BBH-23	(110)	0.3730	1.1043	...	...
	(111)	0.3570	3.6328	...	...
	(220)	0.6434	11.2444	0.5197	12.2165
	(330)	0.9159	11.2855	0.8246	11.8901
BBH-12	(440)	1.1892	11.3026	1.11690	11.6904
	(110)	0.3654	10.9405	...	...
	(111)	0.3485	3.5715	...	...
	(220)	0.6279	11.0667	0.5043	12.0431
	(330)	0.8923	11.10375	0.8016	11.6951
	(440)	1.1574	11.1192	1.0858	11.4945

TABLE VI: QNMs of the remnant Kerr BH in GR, used in the fitting procedure described in Sec IV.



- 
- [1] C. M. Will, The Confrontation between General Relativity and Experiment, *Living Rev. Rel.* **17**, 4 (2014), arXiv:1403.7377 [gr-qc].
- [2] M. Ishak, Testing General Relativity in Cosmology, *Living Rev. Rel.* **22**, 1 (2019), arXiv:1806.10122 [astro-ph.CO].
- [3] J. Aasi *et al.* (LIGO Scientific), Advanced LIGO, *Class. Quant. Grav.* **32**, 074001 (2015), arXiv:1411.4547 [gr-qc].
- [4] F. Acernese *et al.* (VIRGO), Advanced Virgo: a second-generation interferometric gravitational wave detector, *Class. Quant. Grav.* **32**, 024001 (2015), arXiv:1408.3978 [gr-qc].
- [5] B. P. Abbott *et al.* (LIGO Scientific, Virgo), Tests of general relativity with GW150914, *Phys. Rev. Lett.* **116**, 221101 (2016), [Erratum: *Phys.Rev.Lett.* 121, 129902 (2018)], arXiv:1602.03841 [gr-qc].
- [6] B. P. Abbott *et al.* (LIGO Scientific, Virgo), Tests of General Relativity with the Binary Black Hole Signals from the LIGO-Virgo Catalog GWTC-1, *Phys. Rev. D* **100**, 104036 (2019), arXiv:1903.04467 [gr-qc].
- [7] B. P. Abbott *et al.* (LIGO Scientific, Virgo), Tests of General Relativity with GW170817, *Phys. Rev. Lett.* **123**, 011102 (2019), arXiv:1811.00364 [gr-qc].
- [8] R. Abbott *et al.* (LIGO Scientific, Virgo), Tests of general relativity with binary black holes from the second LIGO-Virgo gravitational-wave transient catalog, *Phys. Rev. D* **103**, 122002 (2021), arXiv:2010.14529 [gr-qc].
- [9] R. Abbott *et al.* (LIGO Scientific, VIRGO, KAGRA), Tests of General Relativity with GWTC-3, (2021), arXiv:2112.06861 [gr-qc].
- [10] V. Cardoso and P. Pani, Testing the nature of dark compact objects: a status report, *Living Rev. Rel.* **22**, 4 (2019), arXiv:1904.05363 [gr-qc].
- [11] N. Yunes, K. Yagi, and F. Pretorius, Theoretical Physics Implications of the Binary Black-Hole Mergers GW150914 and GW151226, *Phys. Rev. D* **94**, 084002 (2016), arXiv:1603.08955 [gr-qc].
- [12] T. Baker, E. Bellini, P. G. Ferreira, M. Lagos, J. Noller, and I. Sawicki, Strong constraints on cosmological gravity from GW170817 and GRB 170817A, *Phys. Rev. Lett.* **119**, 251301 (2017), arXiv:1710.06394 [astro-ph.CO].
- [13] Z. Lyu, N. Jiang, and K. Yagi, Constraints on Einstein-dilation-Gauss-Bonnet gravity from black hole-neutron star gravitational wave events, *Phys. Rev. D* **105**, 064001 (2022), arXiv:2201.02543 [gr-qc].
- [14] S. E. Perkins, R. Nair, H. O. Silva, and N. Yunes, Improved gravitational-wave constraints on higher-order curvature theories of gravity, *Phys. Rev. D* **104**, 024060 (2021), arXiv:2104.11189 [gr-qc].
- [15] M. Okounkova, W. M. Farr, M. Isi, and L. C. Stein, Constraining gravitational wave amplitude birefringence and Chern-Simons gravity with GWTC-2, *Phys. Rev. D* **106**, 044067 (2022), arXiv:2101.11153 [gr-qc].
- [16] S. Weinberg, Effective Field Theory for Inflation, *Phys. Rev. D* **77**, 123541 (2008), arXiv:0804.4291 [hep-th].
- [17] A. D. Kovács and H. S. Reall, Well-Posed Formulation of Scalar-Tensor Effective Field Theory, *Phys. Rev. Lett.* **124**, 221101 (2020), arXiv:2003.04327 [gr-qc].
- [18] D. J. Gross and J. H. Sloan, The Quartic Effective Action for the Heterotic String, *Nucl. Phys. B* **291**, 41 (1987).
- [19] B. Zwiebach, Curvature Squared Terms and String Theories, *Phys. Lett. B* **156**, 315 (1985).
- [20] P. A. Cano and A. Ruipérez, String gravity in D=4, *Phys. Rev. D* **105**, 044022 (2022), arXiv:2111.04750 [hep-th].
- [21] P. Kanti, N. E. Mavromatos, J. Rizos, K. Tamvakis, and E. Winstanley, Dilatonic black holes in higher curvature string gravity, *Phys. Rev. D* **54**, 5049 (1996), arXiv:hep-th/9511071.
- [22] T. P. Sotiriou and S.-Y. Zhou, Black hole hair in generalized scalar-tensor gravity: An explicit example, *Phys. Rev. D* **90**, 124063 (2014), arXiv:1408.1698 [gr-qc].
- [23] C. A. R. Herdeiro and E. Radu, Asymptotically flat black holes with scalar hair: A review, *Int. J. Mod. Phys. D* **24**, 1542014 (2015), arXiv:1504.08209 [gr-qc].
- [24] K. Yagi, L. C. Stein, N. Yunes, and T. Tanaka, Post-Newtonian, Quasi-Circular Binary Inspirals in Quadratic Modified Gravity, *Phys. Rev. D* **85**, 064022 (2012), [Erratum: *Phys.Rev.D* 93, 029902 (2016)], arXiv:1110.5950 [gr-qc].
- [25] T. Kobayashi, Horndeski theory and beyond: A review, *Rept. Prog. Phys.* **82**, 086901 (2019), arXiv:1901.07183 [gr-qc].
- [26] W. E. East and J. L. Ripley, Evolution of Einstein-scalar-Gauss-Bonnet gravity using a modified harmonic formulation, *Physical Review D* **103**, 10.1103/physrevd.103.044040 (2021).
- [27] L. Aresté Saló, K. Clough, and P. Figueras, Well-posedness of the four-derivative scalar-tensor theory of gravity in singularity avoiding coordinates, (2022), arXiv:2208.14470 [gr-qc].
- [28] W. E. East and F. Pretorius, Binary neutron star mergers in Einstein-scalar-Gauss-Bonnet gravity, *Phys. Rev. D* **106**, 104055 (2022), arXiv:2208.09488 [gr-qc].
- [29] J. L. Ripley, Numerical relativity for Horndeski gravity, *Int. J. Mod. Phys. D* **31**, 2230017 (2022), arXiv:2207.13074 [gr-qc].
- [30] J. L. Ripley and F. Pretorius, Hyperbolicity in Spherical Gravitational Collapse in a Horndeski Theory, *Phys. Rev. D* **99**, 084014 (2019), arXiv:1902.01468 [gr-qc].
- [31] J. L. Ripley and F. Pretorius, Gravitational collapse in Einstein dilaton-Gauss-Bonnet gravity, *Class. Quant. Grav.* **36**, 134001 (2019), arXiv:1903.07543 [gr-qc].
- [32] A. H. K. R., J. L. Ripley, and N. Yunes, Where and why does Einstein-Scalar-Gauss-Bonnet theory break down?, (2022), arXiv:2211.08477 [gr-qc].
- [33] N. Yunes and X. Siemens, Gravitational-Wave Tests of General Relativity with Ground-Based Detectors and Pulsar Timing-Arrays, *Living Rev. Rel.* **16**, 9 (2013), arXiv:1304.3473 [gr-qc].
- [34] E. Berti, K. Yagi, and N. Yunes, Extreme Gravity Tests with Gravitational Waves from Compact Binary Coalescences: (I) Inspiral-Merger, *Gen. Rel. Grav.* **50**, 46 (2018), arXiv:1801.03208 [gr-qc].
- [35] E. Berti, K. Yagi, H. Yang, and N. Yunes, Extreme Gravity Tests with Gravitational Waves from Compact Binary Coalescences: (II) Ringdown, *Gen. Rel. Grav.* **50**, 49 (2018), arXiv:1801.03587 [gr-qc].

- [36] B. Shiralilou, T. Hinderer, S. Nissanke, N. Ortiz, and H. Witek, Nonlinear curvature effects in gravitational waves from inspiralling black hole binaries, *Phys. Rev. D* **103**, L121503 (2021), arXiv:2012.09162 [gr-qc].
- [37] P. Wagle, A. Saffer, and N. Yunes, Polarization modes of gravitational waves in quadratic gravity, *Physical Review D* **100**, 10.1103/physrevd.100.124007 (2019).
- [38] M. Isi, A. J. Weinstein, C. Mead, and M. Pitkin, Detecting Beyond-Einstein Polarizations of Continuous Gravitational Waves, *Phys. Rev. D* **91**, 082002 (2015), arXiv:1502.00333 [gr-qc].
- [39] M. Isi, M. Pitkin, and A. J. Weinstein, Probing Dynamical Gravity with the Polarization of Continuous Gravitational Waves, *Phys. Rev. D* **96**, 042001 (2017), arXiv:1703.07530 [gr-qc].
- [40] M. Isi and A. J. Weinstein, Probing gravitational wave polarizations with signals from compact binary coalescences, (2017), arXiv:1710.03794 [gr-qc].
- [41] M. Isi, Parametrizing gravitational-wave polarizations, (2022), arXiv:2208.03372 [gr-qc].
- [42] M. Isi and L. C. Stein, Measuring stochastic gravitational-wave energy beyond general relativity, *Phys. Rev. D* **98**, 104025 (2018), arXiv:1807.02123 [gr-qc].
- [43] A. Joyce, B. Jain, J. Khoury, and M. Trodden, Beyond the Cosmological Standard Model, *Phys. Rept.* **568**, 1 (2015), arXiv:1407.0059 [astro-ph.CO].
- [44] E. Berti *et al.*, Testing General Relativity with Present and Future Astrophysical Observations, *Class. Quant. Grav.* **32**, 243001 (2015), arXiv:1501.07274 [gr-qc].
- [45] D. M. Eardley, D. L. Lee, and A. P. Lightman, Gravitational-wave observations as a tool for testing relativistic gravity, *Phys. Rev. D* **8**, 3308 (1973).
- [46] K. Chatziioannou, N. Yunes, and N. Cornish, Model-Independent Test of General Relativity: An Extended post-Einsteinian Framework with Complete Polarization Content, *Phys. Rev. D* **86**, 022004 (2012), [Erratum: *Phys.Rev.D* 95, 129901 (2017)], arXiv:1204.2585 [gr-qc].
- [47] S. Hou, Y. Gong, and Y. Liu, Polarizations of gravitational waves in Horndeski theory, *The European Physical Journal C* **78**, 10.1140/epjc/s10052-018-5869-y (2018).
- [48] D. L. Lee, Conservation laws, gravitational waves, and mass losses in the Dicke-Brans-Jordan theory of gravity, *Phys. Rev. D* **10**, 2374 (1974).
- [49] M. Okounkova, L. C. Stein, M. A. Scheel, and D. A. Hemberger, Numerical binary black hole mergers in dynamical Chern-Simons gravity: Scalar field, *Phys. Rev. D* **96**, 044020 (2017), arXiv:1705.07924 [gr-qc].
- [50] H. Witek, L. Gualtieri, P. Pani, and T. P. Sotiriou, Black holes and binary mergers in scalar Gauss-Bonnet gravity: Scalar field dynamics, *Phys. Rev. D* **99**, 064035 (2019), arXiv:1810.05177 [gr-qc].
- [51] S. W. Hawking, Black holes in the Brans-Dicke theory of gravitation, *Communications in Mathematical Physics* **25**, 167 (1972).
- [52] B. P. Abbott *et al.* (LIGO Scientific, Virgo, Fermi-GBM, INTEGRAL), Gravitational Waves and Gamma-rays from a Binary Neutron Star Merger: GW170817 and GRB 170817A, *Astrophys. J. Lett.* **848**, L13 (2017), arXiv:1710.05834 [astro-ph.HE].
- [53] M. Okounkova, Numerical relativity simulation of GW150914 in Einstein dilaton Gauss-Bonnet gravity, *Phys. Rev. D* **102**, 084046 (2020), arXiv:2001.03571 [gr-qc].
- [54] M. Corman, J. L. Ripley, and W. E. East, Nonlinear studies of binary black hole mergers in Einstein-scalar-Gauss-Bonnet gravity, (2022), arXiv:2210.09235 [gr-qc].
- [55] J. L. Ripley and F. Pretorius, Scalarized Black Hole dynamics in Einstein dilaton Gauss-Bonnet Gravity, *Phys. Rev. D* **101**, 044015 (2020), arXiv:1911.11027 [gr-qc].
- [56] Z. Lyu, N. Jiang, and K. Yagi, Constraints on einstein-dilation-gauss-bonnet gravity from black hole-neutron star gravitational wave events, *Physical Review D* **105**, 10.1103/physrevd.105.064001 (2022).
- [57] L. Amendola, C. Charmousis, and S. C. Davis, Solar System Constraints on Gauss-Bonnet Mediated Dark Energy, *JCAP* **10**, 004, arXiv:0704.0175 [astro-ph].
- [58] R. D. Reasenber, I. I. Shapiro, P. E. MacNeil, R. B. Goldstein, J. C. Breidenthal, J. P. Brenkle, D. L. Cain, T. M. Kaufman, T. A. Komarek, and A. I. Zygielbaum, Viking relativity experiment - Verification of signal retardation by solar gravity, *ApJl* **234**, L219 (1979).
- [59] B. Bertotti, L. Iess, and P. Tortora, A test of general relativity using radio links with the Cassini spacecraft, *Nature* **425**, 374 (2003).
- [60] H.-T. Wang, S.-P. Tang, P.-C. Li, M.-Z. Han, and Y.-Z. Fan, Tight constraints on Einstein-dilation-Gauss-Bonnet gravity from GW190412 and GW190814, *Phys. Rev. D* **104**, 024015 (2021), arXiv:2104.07590 [gr-qc].
- [61] S. Tahura, K. Yagi, and Z. Carson, Testing gravity with gravitational waves from binary black hole mergers: Contributions from amplitude corrections, *Phys. Rev. D* **100**, 104001 (2019).
- [62] G. Carullo, Enhancing modified gravity detection from gravitational-wave observations using the parametrized ringdown spin expansion coefficients formalism, *Phys. Rev. D* **103**, 124043 (2021), arXiv:2102.05939 [gr-qc].
- [63] H. O. Silva, A. Ghosh, and A. Buonanno, Black-hole ringdown as a probe of higher-curvature gravity theories, (2022), arXiv:2205.05132 [gr-qc].
- [64] K. Yagi, New constraint on scalar Gauss-Bonnet gravity and a possible explanation for the excess of the orbital decay rate in a low-mass X-ray binary, *Phys. Rev. D* **86**, 081504 (2012).
- [65] L. C. Stein and K. Yagi, Parametrizing and constraining scalar corrections to general relativity, *Phys. Rev. D* **89**, 044026 (2014).
- [66] P. Pani, E. Berti, V. Cardoso, and J. Read, Compact stars in alternative theories of gravity: Einstein-Dilaton-Gauss-Bonnet gravity, *Phys. Rev. D* **84**, 104035 (2011).
- [67] H. Witek, L. Gualtieri, P. Pani, and T. P. Sotiriou, Black holes and binary mergers in scalar Gauss-Bonnet gravity: Scalar field dynamics, *Phys. Rev. D* **99**, 064035 (2019).
- [68] T. Damour and G. Esposito-Farèse, Nonperturbative strong-field effects in tensor-scalar theories of gravitation, *Phys. Rev. Lett.* **70**, 2220 (1993).
- [69] S. S. Shapiro, J. L. Davis, D. E. Lebach, and J. S. Gregory, Measurement of the Solar Gravitational Deflection of Radio Waves using Geodetic Very-Long-Baseline Interferometry Data, 1979-1999, *Phys. Rev. Lett.* **92**, 121101 (2004).
- [70] T. Andrade, L. A. Salo, J. C. Aurrekoetxea, J. Bamber, K. Clough, R. Croft, E. de Jong, A. Drew, A. Duran, P. G. Ferreira, P. Figueras, H. Finkel, T. França, B.-X.

- Ge, C. Gu, T. Helfer, J. Jäykkä, C. Joana, M. Kunesch, K. Kornet, E. A. Lim, F. Muia, Z. Nazari, M. Radia, J. Ripley, P. Shellard, U. Sperhake, D. Traykova, S. Tunyasuvunakool, Z. Wang, J. Y. Widdicombe, and K. Wong, GRChombo: An adaptable numerical relativity code for fundamental physics, *Journal of Open Source Software* **6**, 3703 (2021).
- [71] K. Clough, P. Figueras, H. Finkel, M. Kunesch, E. A. Lim, and S. Tunyasuvunakool, GRChombo : Numerical Relativity with Adaptive Mesh Refinement, *Class. Quant. Grav.* **32**, 245011 (2015), arXiv:1503.03436 [gr-qc].
- [72] M. Radia, U. Sperhake, A. Drew, K. Clough, P. Figueras, E. A. Lim, J. L. Ripley, J. C. Aurrekoetxea, T. França, and T. Helfer, Lessons for adaptive mesh refinement in numerical relativity, *Class. Quant. Grav.* **39**, 135006 (2022), arXiv:2112.10567 [gr-qc].
- [73] M. A. et al., Tech. Report No. LBNL-6616E (2019).
- [74] D. Alic, C. Bona-Casas, C. Bona, L. Rezzolla, and C. Palenzuela, Conformal and covariant formulation of the Z4 system with constraint-violation damping, *Phys. Rev. D* **85**, 064040 (2012).
- [75] M. Campanelli, C. O. Lousto, P. Marronetti, and Y. Zlochower, Accurate evolutions of orbiting black-hole binaries without excision, *Phys. Rev. Lett.* **96**, 111101 (2006), arXiv:gr-qc/0511048.
- [76] J. G. Baker, J. Centrella, D.-I. Choi, M. Koppitz, and J. van Meter, Gravitational wave extraction from an inspiraling configuration of merging black holes, *Phys. Rev. Lett.* **96**, 111102 (2006), arXiv:gr-qc/0511103.
- [77] D. Alic, W. Kastaun, and L. Rezzolla, Constraint damping of the conformal and covariant formulation of the Z4 system in simulations of binary neutron stars, *Phys. Rev. D* **88**, 064049 (2013).
- [78] T. W. Baumgarte and S. L. Shapiro, On the numerical integration of Einstein's field equations, *Phys. Rev. D* **59**, 024007 (1998), arXiv:gr-qc/9810065.
- [79] M. Shibata and T. Nakamura, Evolution of three-dimensional gravitational waves: Harmonic slicing case, *Phys. Rev. D* **52**, 5428 (1995).
- [80] T. Nakamura, K. Oohara, and Y. Kojima, General Relativistic Collapse To Black Holes And Gravitational Waves From Black Holes, *Prog. Theor. Phys. Suppl.* **90**, 1 (1987).
- [81] S. Brandt and B. Brügmann, A simple construction of initial data for multiple black holes, *Phys. Rev. Lett.* **78**, 3606 (1997).
- [82] J. M. Bowen and J. W. York, Time-asymmetric initial data for black holes and black-hole collisions, *Phys. Rev. D* **21**, 2047 (1980).
- [83] M. Radia, U. Sperhake, E. Berti, and R. Croft, Anomalies in the gravitational recoil of eccentric black-hole mergers with unequal mass ratios, *Phys. Rev. D* **103**, 104006 (2021).
- [84] M. Ansorg, B. Bruegmann, and W. Tichy, A Single-domain spectral method for black hole puncture data, *Phys. Rev. D* **70**, 064011 (2004), arXiv:gr-qc/0404056.
- [85] A. H. Mroue, H. P. Pfeiffer, L. E. Kidder, and S. A. Teukolsky, Measuring orbital eccentricity and periastron advance in quasi-circular black hole simulations, *Phys. Rev. D* **82**, 124016 (2010), arXiv:1004.4697 [gr-qc].
- [86] E. Newman and R. Penrose, An Approach to gravitational radiation by a method of spin coefficients, *J. Math. Phys.* **3**, 566 (1962).
- [87] N. T. Bishop and L. Rezzolla, Extraction of Gravitational Waves in Numerical Relativity, *Living Rev. Rel.* **19**, 2 (2016), arXiv:1606.02532 [gr-qc].
- [88] B. Bruegmann, J. A. Gonzalez, M. Hannam, S. Husa, U. Sperhake, and W. Tichy, Calibration of Moving Puncture Simulations, *Phys. Rev. D* **77**, 024027 (2008), arXiv:gr-qc/0610128.
- [89] Y. Wiaux, L. Jacques, and P. Vanderghelynst, Fast spin  $+2$  spherical harmonics transforms, *J. Comput. Phys.* **226**, 2359 (2007), arXiv:astro-ph/0508514.
- [90] H. Witek, V. Cardoso, C. Herdeiro, A. Nerozzi, U. Sperhake, and M. Zilhao, Black holes in a box: Towards the numerical evolution of black holes in AdS, *Phys. Rev. D* **82**, 104037 (2010), arXiv:1004.4633 [hep-th].
- [91] M. Campanelli and C. O. Lousto, Second order gauge invariant gravitational perturbations of a Kerr black hole, *Phys. Rev. D* **59**, 124022 (1999).
- [92] C. O. Lousto and Y. Zlochower, Practical formula for the radiated angular momentum, *Phys. Rev. D* **76**, 041502 (2007).
- [93] B. Shiralilou, T. Hinderer, S. Nissanke, N. Ortiz, and H. Witek, Post-Newtonian Gravitational and Scalar Waves in Scalar-Gauss-Bonnet Gravity, (2021), arXiv:2105.13972 [gr-qc].
- [94] E. Berti, V. Cardoso, J. A. Gonzalez, U. Sperhake, M. Hannam, S. Husa, and B. Bruegmann, Inspiral, merger and ringdown of unequal mass black hole binaries: A Multipolar analysis, *Phys. Rev. D* **76**, 064034 (2007), arXiv:gr-qc/0703053.
- [95] W. H. Press, Long Wave Trains of Gravitational Waves from a Vibrating Black Hole, *Astrophys. J. Lett.* **170**, L105 (1971).
- [96] E. Berti, V. Cardoso, and A. O. Starinets, Quasinormal modes of black holes and black branes, *Class. Quant. Grav.* **26**, 163001 (2009), arXiv:0905.2975 [gr-qc].
- [97] S. A. Teukolsky, Perturbations of a rotating black hole. 1. Fundamental equations for gravitational electromagnetic and neutrino field perturbations, *Astrophys. J.* **185**, 635 (1973).
- [98] R. A. Konoplya and A. F. Zinhailo, Quasinormal modes, stability and shadows of a black hole in the 4D Einstein-Gauss-Bonnet gravity, *Eur. Phys. J. C* **80**, 1049 (2020), arXiv:2003.01188 [gr-qc].
- [99] A. Bryant, H. O. Silva, K. Yagi, and K. Glampedakis, Eikonal quasinormal modes of black holes beyond general relativity. III. Scalar Gauss-Bonnet gravity, *Phys. Rev. D* **104**, 044051 (2021), arXiv:2106.09657 [gr-qc].
- [100] L. Pierini and L. Gualtieri, Quasinormal modes of rotating black holes in Einstein-dilaton Gauss-Bonnet gravity: The first order in rotation, *Physical Review D* **103**, 10.1103/physrevd.103.124017 (2021).
- [101] L. Pierini and L. Gualtieri, Quasi-normal modes of rotating black holes in Einstein-dilaton Gauss-Bonnet gravity: The second order in rotation, (2022), arXiv:2207.11267 [gr-qc].
- [102] D. Li, P. Wagle, Y. Chen, and N. Yunes, Perturbations of spinning black holes beyond General Relativity: Modified Teukolsky equation, (2022), arXiv:2206.10652 [gr-qc].
- [103] M. Okounkova, L. C. Stein, M. A. Scheel, and S. A. Teukolsky, Numerical binary black hole collisions in dynamical Chern-Simons gravity, *Phys. Rev. D* **100**, 104026 (2019), arXiv:1906.08789 [gr-qc].

- [104] D. Foreman-Mackey, D. W. Hogg, D. Lang, and J. Goodman, emcee: The MCMC Hammer, *PASP* **125**, 306 (2013), 1202.3665.
- [105] L. C. Stein, qnm: A Python package for calculating Kerr quasinormal modes, separation constants, and spherical-spheroidal mixing coefficients, *J. Open Source Softw.* **4**, 1683 (2019), arXiv:1908.10377 [gr-qc].
- [106] S. Bhagwat, M. Okounkova, S. W. Ballmer, D. A. Brown, M. Giesler, M. A. Scheel, and S. A. Teukolsky, On choosing the start time of binary black hole ringdowns, *Phys. Rev. D* **97**, 104065 (2018), arXiv:1711.00926 [gr-qc].
- [107] C. D. Capano, M. Cabero, J. Westerweck, J. Abedi, S. Kastha, A. H. Nitz, Y.-F. Wang, A. B. Nielsen, and B. Krishnan, Observation of a multimode quasinormal spectrum from a perturbed black hole, (2021), arXiv:2105.05238 [gr-qc].
- [108] L. London, D. Shoemaker, and J. Healy, Modeling ringdown: Beyond the fundamental quasinormal modes, *Phys. Rev. D* **90**, 124032 (2014), [Erratum: *Phys. Rev. D* **94**, 069902 (2016)], arXiv:1404.3197 [gr-qc].
- [109] M. Giesler, M. Isi, M. A. Scheel, and S. Teukolsky, Black Hole Ringdown: The Importance of Overtones, *Phys. Rev. X* **9**, 041060 (2019), arXiv:1903.08284 [gr-qc].
- [110] X. Jiménez Forteza, S. Bhagwat, P. Pani, and V. Ferrari, Spectroscopy of binary black hole ringdown using overtones and angular modes, *Phys. Rev. D* **102**, 044053 (2020), arXiv:2005.03260 [gr-qc].
- [111] L. Magaña Zertuche *et al.*, High Precision Ringdown Modeling: Multimode Fits and BMS Frames, *Phys. Rev. D* **105**, 104015 (2022), arXiv:2110.15922 [gr-qc].
- [112] M. Isi and W. M. Farr, Analyzing black-hole ringdowns, (2021), arXiv:2107.05609 [gr-qc].
- [113] R. Cotesta, G. Carullo, E. Berti, and V. Cardoso, Analysis of Ringdown Overtones in GW150914, *Phys. Rev. Lett.* **129**, 111102 (2022), arXiv:2201.00822 [gr-qc].
- [114] M. H.-Y. Cheung *et al.*, Nonlinear effects in black hole ringdown, (2022), arXiv:2208.07374 [gr-qc].
- [115] K. Mitman *et al.*, Nonlinearities in black hole ringdowns, (2021), arXiv:2208.07380 [gr-qc].
- [116] J. Aasi *et al.* (LIGO Scientific), Advanced LIGO, *Class. Quant. Grav.* **32**, 074001 (2015), arXiv:1411.4547 [gr-qc].
- [117] B. P. Abbott *et al.* (KAGRA, LIGO Scientific, Virgo, VIRGO), Prospects for observing and localizing gravitational-wave transients with Advanced LIGO, Advanced Virgo and KAGRA, *Living Rev. Rel.* **21**, 3 (2018), arXiv:1304.0670 [gr-qc].
- [118] M. Punturo *et al.*, The Einstein Telescope: A third-generation gravitational wave observatory, *Class. Quant. Grav.* **27**, 194002 (2010).
- [119] S. Hild *et al.*, Sensitivity Studies for Third-Generation Gravitational Wave Observatories, *Class. Quant. Grav.* **28**, 094013 (2011), arXiv:1012.0908 [gr-qc].
- [120] B. P. Abbott *et al.* (LIGO Scientific, Virgo), Search for intermediate mass black hole binaries in the first observing run of Advanced LIGO, *Phys. Rev. D* **96**, 022001 (2017), arXiv:1704.04628 [gr-qc].
- [121] F. Iacovelli, M. Mancarella, S. Foffa, and M. Maggiore, Forecasting the detection capabilities of third-generation gravitational-wave detectors using GWFAST, (2022), arXiv:2207.02771 [gr-qc].
- [122] B. P. Abbott and *et al.* (LIGO Scientific Collaboration and Virgo Collaboration), GW151226: Observation of gravitational waves from a 22-solar-mass binary black hole coalescence, *Phys. Rev. Lett.* **116**, 241103 (2016).
- [123] R. Abbott *et al.* (LIGO Scientific, Virgo), GWTC-2: Compact Binary Coalescences Observed by LIGO and Virgo During the First Half of the Third Observing Run, *Phys. Rev. X* **11**, 021053 (2021), arXiv:2010.14527 [gr-qc].
- [124] G. Carullo, W. Del Pozzo, and J. Veitch, Observational Black Hole Spectroscopy: A time-domain multimode analysis of GW150914, *Phys. Rev. D* **99**, 123029 (2019), [Erratum: *Phys. Rev. D* **100**, 089903 (2019)], arXiv:1902.07527 [gr-qc].
- [125] M. Isi, M. Giesler, W. M. Farr, M. A. Scheel, and S. A. Teukolsky, Testing the no-hair theorem with GW150914, *Phys. Rev. Lett.* **123**, 111102 (2019), arXiv:1905.00869 [gr-qc].
- [126] J. Skilling, Nested Sampling, in *Bayesian Inference and Maximum Entropy Methods in Science and Engineering: 24th International Workshop on Bayesian Inference and Maximum Entropy Methods in Science and Engineering*, American Institute of Physics Conference Series, Vol. 735, edited by R. Fischer, R. Preuss, and U. V. Toussaint (2004) pp. 395–405.
- [127] W. D. Pozzo and J. Veitch, CPNest: An efficient PYTHON parallelizable nested sampling algorithm, *Astrophysics Source Code Library*, record ascl:2205.021 (2022), ascl:2205.021.
- [128] P. Schmidt, I. W. Harry, and H. P. Pfeiffer, Numerical Relativity Injection Infrastructure, (2017), arXiv:1703.01076 [gr-qc].
- [129] LIGO Scientific Collaboration, LIGO Algorithm Library - LALSuite, free software (GPL) (2018).
- [130] S. Borhanian and B. S. Sathyaprakash, Listening to the Universe with Next Generation Ground-Based Gravitational-Wave Detectors, (2022), arXiv:2202.11048 [gr-qc].
- [131] A. Zimmerman, C.-J. Haster, and K. Chatziioannou, On combining information from multiple gravitational wave sources, *Phys. Rev. D* **99**, 124044 (2019).
- [132] P. Amaro-Seoane *et al.* (LISA), Laser Interferometer Space Antenna, (2017), arXiv:1702.00786 [astro-ph.IM].
- [133] R. Benkel, T. P. Sotiriou, and H. Witek, Dynamical scalar hair formation around a Schwarzschild black hole, *Phys. Rev. D* **94**, 121503 (2016), arXiv:1612.08184 [gr-qc].
- [134] H. O. Silva, H. Witek, M. Elley, and N. Yunes, Dynamical Descalarization in Binary Black Hole Mergers, *Phys. Rev. Lett.* **127**, 031101 (2021), arXiv:2012.10436 [gr-qc].
- [135] I. Kamaretsos, M. Hannam, and B. Sathyaprakash, Is black-hole ringdown a memory of its progenitor?, *Phys. Rev. Lett.* **109**, 141102 (2012), arXiv:1207.0399 [gr-qc].
- [136] L. T. London, Modeling ringdown. II. Aligned-spin binary black holes, implications for data analysis and fundamental theory, *Phys. Rev. D* **102**, 084052 (2020), arXiv:1801.08208 [gr-qc].